Time- and angle-resolved photoelectron spectroscopy of strong-field light-dressed solids: Prevalence of the adiabatic band picture

Ofer Neufeld [1,*] Wenwen Mao,[1] Hannes Hübener [1] Nicolas Tancogne-Dejean [1] Shunsuke A. Sato [1,2]
Umberto De Giovannini [1,3] and Angel Rubio [1,4,†]

[1]*Max Planck Institute for the Structure and Dynamics of Matter and Center for Free-electron Laser Science, Hamburg 22761, Germany*
[2]*Center for Computational Sciences, University of Tsukuba, Tsukuba 305-8577, Japan*
[3]*Università degli Studi di Palermo, Dipartimento di Fisica e Chimica—Emilio Segrè, Palermo I-90123, Italy*
[4]*Center for Computational Quantum Physics (CCQ), The Flatiron Institute, New York, New York 10010, USA*

In recent years, strong-field physics in condensed matter was pioneered as a potential approach for controlling material properties through laser dressing, as well as for ultrafast spectroscopy via nonlinear light-matter interactions (e.g., harmonic generation). A potential controversy arising from these advancements is that it is sometimes vague which band picture should be used to interpret strong-field experiments: The field-free bands, the adiabatic (instantaneous) field-dressed bands, Floquet bands, or some other intermediate picture. Here, we try to resolve this issue by performing theoretical experiments of time- and angle-resolved photoelectron spectroscopy (Tr-ARPES) for a strong-field laser-pumped solid, which should give access to the actual observable bands of the irradiated material. To our surprise, we find that the adiabatic band picture survives quite well up to high field intensities ($\sim 10^{12}$ W/cm^2) and in a wide frequency range (driving wavelengths of 4000 to 800 nm, with Keldysh parameters ranging up to ~ 7). We conclude that, to first order, the adiabatic instantaneous bands should be the standard blueprint for interpreting ultrafast electron dynamics in solids when the field is highly off resonant with characteristic energy scales of the material. We then discuss weaker effects of modifications of the bands beyond this picture that are nonadiabatic, showing that by using bichromatic fields the deviations from the standard picture can be probed with enhanced sensitivity. In this paper, we outline a clear band picture for the physics of strong-field interactions in solids, which should be useful for designing and analyzing strong-field experimental observables and to formulate simpler semi-empirical models.

I. INTRODUCTION

When solids are irradiated by strong laser pulses, a plethora of physical effects can be initiated. For instance, these can include high harmonic generation (HHG) [1,2], creation of transient injection currents [3–8], the dynamical Franz-Keldysh effect [9,10], and creation of laser-dressed states of matter [11–13]. Depending on the symmetries of the solid and the properties of the laser field, one can even create transient topological phases [12,14] or valley-polarization by selectively populating certain regions of the Brillouin zone [13,15–18]. These phenomena are of technological importance for quantum information processing and petahertz electronics [19] since they allow us to generate and probe ultrafast motion of electrons in solids in real-time. Of particular interest are

*oneufeld@schmidtsciencefellows.org
†angel.rubio@mpsd.mpg.de

topological [20–27] and strongly correlated [28–32] phases since these could hold the key for applications.

What is common in these effects is that they all occur under the same electronic conditions—strong-field driving of a periodic system. However, each effect is usually analyzed in terms of a different band picture to rationalize the results and physical mechanisms. For instance, the mechanism of HHG is usually described with semiclassical models employing the field-free bands [33–42], which are utilized for HHG spectroscopy of various basic electronic properties such as band structure Berry curvatures and density of states [43–47]. The dynamical Franz-Keldysh effect can be interpreted, on the other hand, with a Floquet time-averaged picture for the field-dressed bands [9,10,48–50]. For longer wavelength driving, one might employ an adiabatic band picture based on the instantaneous states of the laser-dressed system, the so called Houston states [51,52], which is useful to obtain insight about vector-potential-induced shifting of the bands [53]. Lastly, some phenomena require an intermediate picture that is neither fully time averaged in the Floquet sense nor instantaneous like the Houston states, which was recently utilized for measuring transient gap closings in higher conduction bands [54]. On the other hand, there are works demonstrating that, in the same conditions, there can be very strong modification of the band structure due to the laser driving itself. For

resonant interactions in the weak-field regime, this approach is known to yield Floquet topological insulators [14]. Naturally, strong-field driving can also yield similar topological phases where the gap of the system substantially changes [13]. It might even induce other phases such as free-electron-like states [12,55,56] or cases where the band structure in higher bands changes (e.g. gaps close) [54]. In these cases, one might say that the choice of how to interpret experiments and formulate models for the electron dynamics is somewhat vague—after all, even if any full basis set can still be used for formulating a model, there is no point in describing electron trajectories in bands if those bands do not exist or alter strongly over time. Similarly, it might be confusing to use dressed bands for describing phases of matter if the underlying electron dynamics are well captured by the field-free bands. We emphasize that the complication arises since several of the effects can coexist because they are driven in the same conditions (they are just described by different observables). Beyond this, it is still an open question up to what laser powers, driving wavelengths, and Keldysh parameters the band picture holds, i.e., do the band shapes significantly change in the strong-field regime (but still below the material damage threshold)?

One possible solution is to employ time- and angel-resolved photoelectron spectroscopy (Tr-ARPES) [57–59]. This approach allows us to directly image populated single-particle bands in periodic systems even if they are simultaneously interacting with strong lasers [60,61]. The advantage here is that the bands themselves become the observable quantities rather than the basis set used for interpreting the experiment. ARPES has already been successfully employed for probing the electronic structure of many systems [62], including topological insulators and Weyl semimetals [63], superconductors [64], and valley pseudospin [65,66]. It has also been utilized for probing dynamical phenomena such as photocurrents in topological insulators [67] and electron-phonon couplings [68–70]. However, it has not yet been employed for investigating a solid system dressed by a strong laser field, which might provide new insights.

Here, we perform *ab initio* calculations of numerical experiments of Tr-ARPES in a periodic system that is dressed by intense laser light. Specifically, we explore a monolayer of hexagonal boron nitride (hBN) as a benchmark system and investigate an instantaneous regime (that probes the instantaneous field-dressed bands) and a Floquet regime (that probes the Floquet cycle-averaged bands). We find that the instantaneous band picture holds up extremely well in strong-field driving—there is no observable breakdown of the bands or strong modification of the energy scales even in conditions where harmonics up to ∼25 eV are driven (driving powers of ∼10^{12} W/cm^2) and in wavelengths ranges of 4000 to 800 nm (Keldysh parameters <7). That is to say that the band picture persists, even far away from what is standardly considered as the adiabatic regime with Keldysh parameters <1. The main effect of the driving is seen to tune the phases of the electronic states (which affects transition matrix elements) and to shift the band origin with the instantaneous vector potential (as explained by the adiabatic theory) [51,52]. We also find that some modifications of the bands arise beyond this instantaneous picture, i.e., involving electron dynamics

that are nonadiabatic. These are slightly weaker effects but should be experimentally detectable. We further show that, by using a bichromatic dressing field, the nonadiabaticity can be probed with enhanced sensitivity.

The paper is ordered as follows: In Sec. II, we present the methodology of our *ab initio* calculations, also detailing how to remove contributions of continuum electron acceleration from the analysis. Section III outlines the logic of numerical experiments of Tr-ARPES from strongly driven solids, outlining different regimes of laser parameters as well as some of the expected band pictures as predicted from various theories. Section IV presents the main results and analysis, showing field-dressed bands under various driving conditions, including both Floquet and instantaneous regimes, and discussing adiabatic and nonadiabatic effects. Section V presents Tr-ARPES from bichromatically strong-field driven systems with emphasis on nonadiabatic light-dressing effects. Finally, Sec. VI summarizes our results.

II. METHODOLOGY

A. Laser-driven dynamics

We begin by outlining the methodology of our *ab initio* calculations. All results are obtained with the open-access real-space grid-based code OCTOPUS [71–74]. The dynamics of electrons with impinging laser light are described within the framework of real-time time-dependent density functional theory (TDDFT) [75] and within the adiabatic approximation for the exchange correlation (XC) functional (in the local density approximation). The laser-matter interaction is described in the velocity gauge, where the ions are assumed to be frozen and noninteracting with the laser field (which should be a valid approximation on few-femtosecond timescales). We also neglect any macroscopic effects of phase matching and laser pulse propagation in the material. The resulting equations of motion for the Kohn-Sham (KS) Bloch states are given by (we use atomic units throughout, unless stated otherwise)

$$i\partial_t \left| \varphi_{n,k}^{KS}(t) \right\rangle = \left\{ \frac{1}{2}\left[-i\nabla + \frac{\mathbf{A}(t)}{c} \right]^2 + v_{KS}(\mathbf{r}, t) \right\} \left| \varphi_{n,k}^{KS}(t) \right\rangle, \quad (1)$$

where $\left| \varphi_{n,k}^{KS}(t) \right\rangle$ is the KS Bloch state at k-point k and band index n, $\mathbf{A}(t)$ is the total vector potential of all laser pulses interacting with matter within the dipole approximation, such that $-\partial_t \mathbf{A}(t) = c\mathbf{E}(t)$, and c is the speed of light in atomic units ($c \approx 137.036$). Here, $v_{KS}(\mathbf{r}, t)$ in Eq. (1) is the time-dependent KS potential given by:

$$v_{KS}(\mathbf{r}, t) = -\sum_I \frac{Z_I}{|\mathbf{R}_I - \mathbf{r}|} + \int d^3r' \frac{n(\mathbf{r}'t)}{|\mathbf{r} - \mathbf{r}'|} + v_{XC}[n(\mathbf{r}, t)], \tag{2}$$

where Z_I is the charge of the Ith nuclei and $\mathbf{R}_I$ is its coordinate, and v_{XC} is the XC potential that is a functional of $n(\mathbf{r}, t) = \sum_{n,k} |\langle \mathbf{r} | \varphi_{n,k}^{KS}(t) \rangle|^2$, the time-dependent electron density. We note that, practically, the bare Coulomb interaction of electrons with the nuclei is replaced with nonlocal pseudopotentials to reduce numerical costs (assuming the frozen core approximation for deep atomic states).

Following Eqs. (1) and (2), the KS Bloch wave functions are propagated in time, where the initial states are taken as the
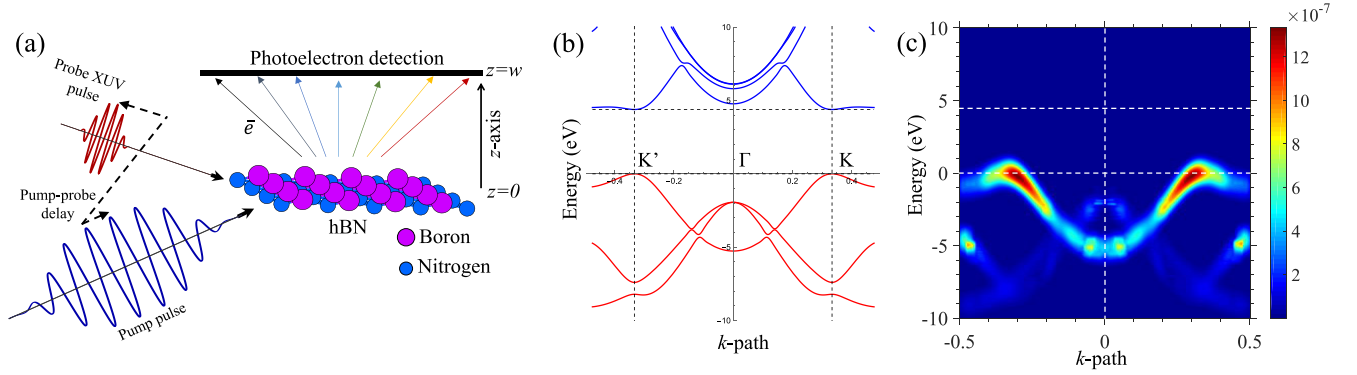
FIG. 1. (a) Illustration of time- and angle-resolved photoelectron spectroscopy (Tr-ARPES) with strong-field setup. A monolayer of hexagonal boron nitride (hBN) is irradiated by an intense pump pulse that is polarized in the monolayer plane (blue), which dresses the electronic system and potentially causes some band modifications. A delayed extreme ultraviolet (XUV) probe pulse that is polarized transverse to the monolayer (along the z axis) then photo-ionizes electrons into the continuum. The photoemitted electrons propagate up to the detector surface, at which point their momenta and energy is recorded. (b) Ground-state density functional theory (DFT) band structure along the K'-Γ-K path. The top of the valence band is set to zero energy, and K and K' points are indicated with dashed lines. Occupied bands are denoted by red lines, while unoccupied bands with blue lines. (c) Pump-free ARPES spectra that capture the details of the equilibrium occupied bands. The energy of the ARPES spectrum is offset by ω_{xuv}, and dashed white lines indicate the positions of the valence and conduction band edges and Γ point.

ground state which is found within density functional theory (DFT). All technical details of the propagation scheme and DFT calculations are delegated to the Appendix.

B. ARPES calculations

To obtain ARPES spectra, we follow the path of performing numerical experiments, which effectively simulate the measurement process as it would occur in the lab (to the best currently possible extent). In this respect, the total vector potential in Eq. (1) that is used for propagating the KS states is split to two:

$$\mathbf{A}(t) = \mathbf{A}_{pump}(t) + \mathbf{A}_{probe}(t). \qquad (3)$$

Here, $\mathbf{A}_{pump}(t)$ refers to the strong-laser field that dresses the system. This field is taken to have the form:

$$\mathbf{A}_{pump}(t) = f(t) \frac{cE_0}{\omega} \sin(\omega t)\hat{\mathbf{e}}, \qquad (4)$$

where $f(t)$ is an envelope function (see Appendix for details), E_0 is the field amplitude, ω is the carrier frequency, and $\hat{\mathbf{e}}$ is a unit vector pointing transversely to the B-N bond axis (along the Γ-K line in reciprocal space) within the monolayer plane (xy plane). The probe pulse $\mathbf{A}_{probe}(t)$ is taken as a linearly polarized pulse polarized along the z axis (transverse to the monolayer), with an extreme ultraviolet (XUV) carrier frequency:

$$\mathbf{A}_{probe}(t) = f_{xuv}(t - t_0) \frac{cE_{xuv}}{\omega_{xuv}} \sin(\omega_{xuv} t)\hat{\mathbf{z}}, \qquad (5)$$

where $f_{xuv}(t)$ is an envelope function with a maximum at $t = 0$, t_0 indicates the pump-probe delay, ω_{xuv} is the probe photon frequency taken here at 100 eV to obtain high temporal resolution, and E_{xuv} is the amplitude of the probe which is taken in the weak-field linear-response regime, corresponding to an intensity of 10^8 W/cm^2. Thus, the pump laser field in Eq. (4) effectively dresses the solid, potentially causing some

modification of the band structure, and the probe in Eq. (5) describes an XUV isolated pulse that photo-ionizes electrons which are then recorded in a momentum-resolved manner as the ARPES spectra. We note that the pump-probe delay t_0 will be referred to from this point on as t_{ion}, which indicates a particular moment in time where f_{xuv} is maximized (leading to the highest probability for photoemission) with respect to $\mathbf{A}_{pump}(t)$. For example, the notation $\mathbf{A}_{pump}(t_{ion}) = 0$ indicates that t_0 is set such that f_{xuv} is maximized when $\mathbf{A}_{pump} = 0$ but closest to the center of the pump pulse [i.e., closest to where $f(t)$ is maximized]. Figure 1(a) summarizes the schematic of the setup.

The ARPES spectra are calculated directly from the propagated KS states and, without additional fundamental assumptions, using the highly accurate and efficient surface-flux method t-SURFF [76,77]. Here, the momentum-resolved flux of photoelectrons is recorded across a surface normal to the hBN monolayer (located at $z = 0$), which lies sufficiently far away in the continuum to avoid interactions of outgoing waves with the monolayer (the surface is located at the plane $z = w$). The photoemission from all KS Bloch states is coherently summed, producing k-resolved spectra along high-symmetry axes. For hBN, we calculate ARPES along a path in reciprocal space that traverses from Γ to K and K' [which is also taken as the pump laser driving axis in Eq. (4)]. Exemplary ARPES spectra for the field-free case (with $E_0 = 0$) can be seen in Fig. 1(c), side-by-side with the field-free band structure obtained with DFT [Fig. 1(b)]. Additional technical details can be found in the Appendix.

C. Removing continuum effects

One issue with this approach (and corresponding experimental setup) is that substantial modifications to the Tr-ARPES spectra might arise from propagation of the photoelectrons in the continuum up to the detector (e.g., laser-assisted photoemission [78,79]) rather than from the
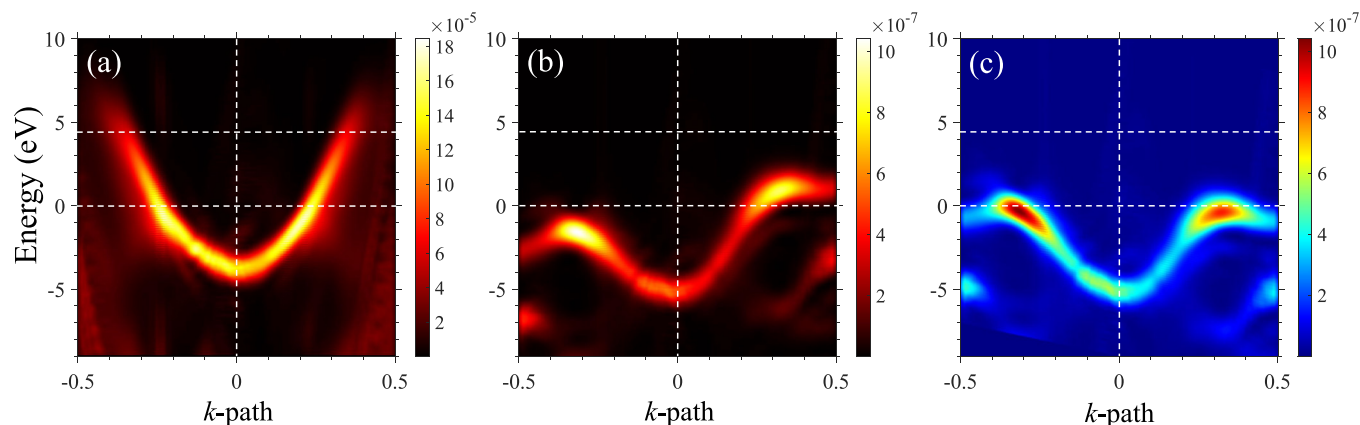
FIG. 2. Continuum effects in strong-field dressed time- and angle-resolved photoelectron spectroscopy (Tr-ARPES) at a pump-probe delay that corresponds to $\mathbf{A}(t_{\mathrm{ion}}) = 0$. (a) Tr-ARPES spectrum from hexagonal boron nitride (hBN) including full propagation in the continuum. (b) Tr-ARPES spectrum from hBN including only propagation in the continuum within the simulation box, from $z = 0$ to $z = w$. The propagation beyond $z = w$ is not performed (see text). (c) Tr-ARPES spectrum from hBN after removing continuum effects according to the two procedures outlined in the text. All Tr-ARPES spectra are calculated in the instantaneous regime (see text) with the parameters $I_0 = 10^{12}$ W/cm^2, $\lambda = 2000$ nm. A different color scale is used for the case where all continuum effects have been removed to indicate that it represents the approximate energy spectrum of the electrons inside the dressed solid. Dashed white lines indicate the positions of the valence and conduction band edges and the Γ point.

light-driven states inside matter. Sometimes these effects comprise a main physical result (e.g., in photoemission from atomic and molecular species [80]). Here however, we are interested in uncovering the nature of the field-dressed bands in the solid, and continuum-related phenomena can be considered as spurious effects that should be artificially removed. This can be a cumbersome procedure because it essentially requires that $\mathbf{A}_{\mathrm{pump}}(t)$ should only be active in a certain region of the simulation box that is localized around the monolayer. One potential solution could be to multiply $\mathbf{A}_{\mathrm{pump}}(t)$ by a spatial envelope, but this is not applicable in the dipole approximation and presents additional complications.

Therefore, we employ two other procedures to remove continuum effects from ARPES spectra. First, the photoelectrons that reach the numerical detector (the surface through which the flux is calculated) are not further propagated in time, but rather, their momenta are recorded at that exact moment. This is a different approach than that usually employed in surface-flux methods, where the photoelectrons are further propagated under the full vector potential as Volkov states (assuming a strong-field approximation) [76,81]. This procedure guarantees that continuum-related effects correspond only to the laser-driven acceleration in the spatial region spanning from the monolayer up to the detector, which should be small because that region is only 30 Bohr wide. An exemplary result of this approach can be seen in Figs. 2(a) and 2(b) which compare field-dressed Tr-ARPES spectra with/without propagation of the Volkov states. From comparing Figs. 2(a) and 2(b), propagation of electrons in the continuum causes substantial modifications of the ARPES spectra. These modifications will be discussed in more detail in the next subsection.

Notably, because E_0 in $\mathbf{A}_{\mathrm{pump}}$ is so large in the strong-field regime, continuum-related effects can still arise after performing the procedure described above—photoelectrons can still accelerate in the xy plane (because they interact

with $\mathbf{A}_{\mathrm{pump}}$) during their propagation up to the detector. For instance, one still observes some linear sloping of the bands in Fig. 2(b), which could partially arise from continuum acceleration rather than from laser dressing of the solid (because laser-induced acceleration adds a term linearly proportional to $\mathbf{k}$ in the photoelectron energy, see below). Therefore, we employ a second procedure to remove such effects—we assume that, in the region spanning from the monolayer up to the detector, the electrons propagate semiclassically, such that their overall momentum is varied by $\mathbf{\Delta A}$:

$$\mathbf{\Delta A}(t_{\mathrm{ion}}) = -c \int_{t_{\mathrm{ion}}}^{t_{\mathrm{ion}}+\Delta t} \mathbf{E}_{\mathrm{pump}}(t)\,dt, \qquad (6)$$

where t_{ion} indicates the approximate moment of ionization (taken here as the time that maximizes $\mathbf{A}_{\mathrm{probe}}(t)$, assuming instantaneous ionization), Δt corresponds to the semiclassical time of flight of the photoelectron as it traverses from $z = 0$ at the monolayer up to the detector at $z = w$, and $\mathbf{E}_{\mathrm{pump}}(t)$ is the electric field associated with $\mathbf{A}_{\mathrm{pump}}(t)$, $c\mathbf{E}_{\mathrm{pump}}(t) = -\partial_t \mathbf{A}_{\mathrm{pump}}(t)$. Here, Δt is calculated assuming semiclassical dynamics under the strong-field approximation—the velocity component of the outgoing electron along the z axis is taken as a constant of motion:

$$v_z = \sqrt{2\omega_{\mathrm{xuv}}}, \qquad (7)$$

such that $\Delta t = w/v_z$. Following this, the ARPES spectra can be artificially subtracted with the energy term $\mathbf{k} \cdot \mathbf{\Delta A}(t_{\mathrm{ion}})/c$, were $\mathbf{k}$ denotes the crystal momentum. The result of this procedure can be seen in Fig. 2(c), which further corrects the main linear slope in the bands seen in Fig. 2(b).

Importantly, the second procedure that subtracts propagation effects in the simulation box can only be performed if a singular well-defined moment of ionization with respect to $\mathbf{A}_{\mathrm{pump}}(t)$ exists. This only occurs in a regime where the probe pulse duration is much shorter than a laser cycle (see

below). Thus, the second correction is not applied to the Floquet-regime calculations outlined below (where the probe pulse duration is longer than a laser cycle). We also emphasize that it is still an approximate procedure because it neglects interactions of the outgoing electron with the monolayer, with the other electrons, and assumes semiclassical motion. Moreover, we have assumed an instantaneous moment of photo-ionization and neglected possible time delays [82,83]. Still, errors arising from this approximation are expected to be small because: (i) ω_{xuv} is taken to be very large (100 eV), which minimizes the time of flight of photoelectrons to ~200 as, and (ii) such effects are anyways usually quite small.

D. Continuum effects

At this point, we briefly discuss some of the continuum-related effects that can occur in the calculation of Tr-ARPES involving strong fields. This discussion is especially important considering the context for this paper—if one does not take extra care in removing these effects, it may seem as though unique phases of matter are measured, while modifications of the bands could just result from continuum dressing.

As an example, we highlight some continuum effects in Fig. 2: Fig. 2(a) presents Tr-ARPES spectra in the standard conditions, where outgoing waves include all of the continuum effects, and the pump-probe delay is set such that $\mathbf{A}(t_{ion}) = 0$. For this pump-probe delay, the instantaneous adiabatic band picture corresponds to field-free system (because $\mathbf{A} \cong 0$ when the photoelectron is ionized), such that the predicted Houston states coincide with the field-free states. However, as clearly visible, the Tr-ARPES spectra shows a parabolic band dispersion along the pump laser polarization axis. The band energies strongly deviate from the field-free system, especially around the K and K' points at the valence band maxima (VBM), seemingly predicting a closing of the bandgap. If one were to interpret this measurement without postprocessing at face value, it would suggest that the strong field induces a free-electron-like state inside the material. However, as is obvious from Fig. 2(b), this free-electron-like state is only present in the dressed continuum. Moreover, deeper-lying bands also exhibit this behavior (not shown), clearly indicating that the parabolic bands originate from continuum acceleration of photoelectrons and not from a laser modification of the solid, which would not affect all the bands equally. Similarly, other phenomena may appear for other pump-probe delays, which could be perceived as fingerprints of unique light-driven phases, such as band bending or widening. We stress that extra caution must be taken before analyzing such phenomena, as they might result from continuum-based effects, even after most continuum effects have been artificially removed. For instance, some band widening along the energy axis is expected due to the nonsingular ionization times of photoelectrons. That is, because electrons can also be ionized slightly before or after the assumed t_{ion}, variations in $\mathbf{\Delta A}$ can be incurred as the outgoing waves propagate to the detector, which cannot be fully subtracted out of the ARPES spectra.

From an experimental standpoint, one may not consider such effects as spurious, but rather, the realistic result of the measurement process. In that respect, the untreated

experimental ARPES data would correspond to the numerical results in Fig. 2(a), i.e., there would hardly be any resemblance to the band picture hiding within. On the other hand, those internal features are often the main goal of the experiment, so in our view, anything obscuring them should be removed. To extract that picture from the measurement, the data would have to be processed, though at this point, we do not know yet how such a procedure might look like, which should be explored in future work.

In an effort to clarify some of these effects, all ARPES spectra in this paper that present the physical field-dressed bands are represented in blue-red colormaps. ARPES spectra that include some continuum effects that have not been subtracted with the two procedures described above are represented by orange-black colormaps. We emphasize that some weaker continuum-related effects might be present even in the ARPES spectra that have undergone the continuum-removal procedures.

III. DRESSED-BAND PICTURES AND LASER REGIMES

Having outlined the methodological approach, we now detail the different possible electronic band pictures for interpreting the dynamics and the physical regimes of interest. We also analyze the main degrees of freedom in $\mathbf{A}_{pump}(t)$ and $\mathbf{A}_{probe}(t)$ and their effect on the resulting spectra.

First, we outline two regimes in which Tr-ARPES is employed in this paper. The first regime is denoted as the *instantaneous regime*. Here, the probe pulse is very short compared with the laser cycle of $\mathbf{A}_{pump}(t)$. Practically, this means that we have

$$\text{FWHM}_{xuv} \ll \frac{2\pi}{\omega}, \tag{8}$$

where FWHM_{xuv} is the full width at half maximum of the probe pulse. An illustration for this regime can be seen in Fig. 3(a)—the probe pulse samples a specific time in the pumped system. The resulting ARPES spectra should then roughly correspond to the band structure of the system in that moment, whatever that may be. The main idea is that, in this way, one may probe the actual physical states in the system as it interacts with $\mathbf{A}_{pump}(t)$ and resolve any ambiguity that arises from the theory one uses to define the state of the system.

The second regime is denoted as the *Floquet regime*. In this regime, the probe pulse duration is on a similar order of magnitude as (or larger than) the pump laser cycle:

$$\text{FWHM}_{xuv} \approx \frac{2\pi}{\omega}. \tag{9}$$

Here, one cannot assign a specific moment of ionization to photoelectrons with respect to the laser cycle, but rather, electrons are emitted continuously throughout different times along the pump field. The photoemission from all these moments is summed coherently, yielding a type of cycle-averaged band picture, which should correspond to the Floquet limit of the field-dressed system [see Fig. 3(b) for illustration].

In terms of extracting physical interpretations from the Tr-ARPES spectra, there could be several contradicting pictures. On the one hand, we have the adiabatic Houston state picture [51,52]. The Houston states are obtained by diagonalizing the
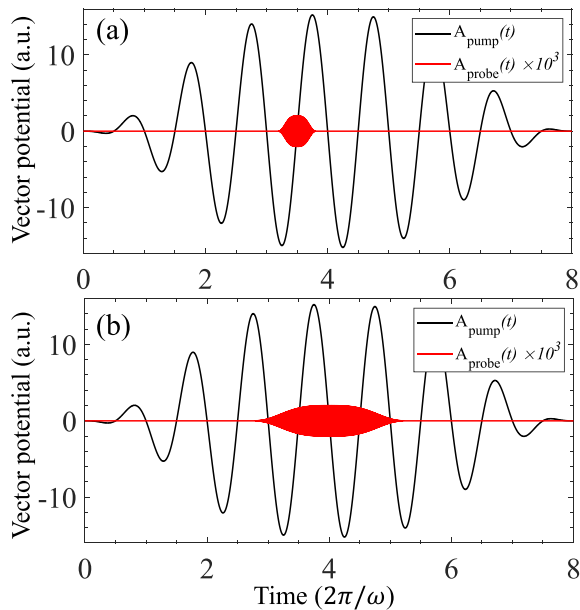
FIG. 3. Illustration of the time- and angle-resolved photoelectron spectroscopy (Tr-ARPES) regimes. (a) Instantaneous regime: The probe pulse has a duration much shorter than the pump field's optical cycle. In this exemplary case, the pump-probe delay is set such that the probe overlaps with a momentary zero in the vector potential, i.e., $\mathbf{A}_{\mathrm{pump}}(t_{\mathrm{ion}}) = 0$. (b) Floquet regime: The probe pulse duration is like one optical cycle of the pump field. Note that the probe pulse amplitude is many orders of magnitude weaker than the pump amplitude but is plotted here on the same scale for clarity.

instantaneous Hamiltonian, including the pump vector potential only, i.e., within our TDDFT approach, one may write

$$\left\{ \frac{1}{2}\left[-i\nabla + \frac{\mathbf{A}_{\mathrm{pump}}(t')}{c}\right]^2 + v_{\mathrm{KS}}(\mathbf{r}, t') \right\} \left|\varphi_{n,k}^{\mathrm{H-KS}}(t')\right\rangle$$
$$= \epsilon_{n,k}^{\mathrm{KS}}(t')\left|\varphi_{n,k}^{\mathrm{H-KS}}(t')\right\rangle, \tag{10}$$

where $\left|\varphi_{n,k}^{\mathrm{H-KS}}\right\rangle$ are the adiabatic Houston-KS Bloch states, with corresponding eigenenergies $\epsilon_{n,k}^{\mathrm{KS}}(t')$, and t' is the

instantaneous moment in time where the diagonalization procedure is performed. We emphasize that Eq. (10) is not solved with time propagation of the initial states up to t' but rather is diagonalized at t' to yield the instantaneous adiabatic band structure (which is time dependent). If the dynamics are exactly adiabatic, then this procedure should be identical to the time propagation up to an overall phase, the Berry phase [84], which interestingly can be indeed inferred from this picture [85]. The main effects of the Houston picture on the bands are twofold: (i) the reference crystal momentum $\mathbf{k}$ is translated by the instantaneous pump vector potential, such that $\mathbf{k} \rightarrow \mathbf{k}' = \mathbf{k} + \mathbf{A}_{\mathrm{pump}}(t')/c$ [53]. This can be considered equivalent to intraband acceleration that is a main step in solid HHG. (ii) The eigenstates can acquire an additional $\mathbf{k}$-dependent and t'-dependent phase. The acquired phase alters the transition matrix elements from the Bloch states to the continuum, which should modulate the photoemission probability vs $\mathbf{k}$. Most notably, for the moments in time where $\mathbf{A}_{\mathrm{pump}}(t') = 0$, the Houston states correspond exactly to the field-free eigenstates up to the Berry phase, neglecting effects of dynamical correlations. This suggests an easy procedure to extract deviations from adiabaticity and/or Berry phases by measuring Tr-ARPES spectra with pump-probe delays for which $\mathbf{A}_{\mathrm{pump}}(t_{\mathrm{ion}}) = 0$ and subtracting it from the field-free ARPES spectra. In this context, the degree of adiabaticity of a system is usually estimated with a Keldysh parameter: $\gamma = \omega\sqrt{2E_g}/E_0$, where E_g is the bandgap. For $\omega \rightarrow 0$ (long-wavelength limit), one might expect that the electrons follow the instantaneous pump field, and the adiabatic picture would hold ($\gamma < 1$). On the other hand, for shorter wavelengths, even if E_0 is large, one can expect deviations from adiabaticity ($\gamma > 1$).

On the opposing side to the instantaneous picture, we have the Floquet picture, which is often employed for analyzing field-driven dynamics [13,14,48,86–89]. Here, the effective bands of the field-dressed system correspond to a time-averaged picture. Assuming perfect temporal periodicity in the pump field [neglecting $f(t)$ in Eq. (4)], one can obtain the Floquet-Bloch Hamiltonian [90], which in the TDDFT picture takes the form:

$$H_f^{\mathrm{KS}} = \log\left[\hat{T}\exp\left(-i\frac{\omega}{2\pi}\int_0^{2\pi/\omega} dt\left\{\frac{1}{2}\left[-i\nabla + \frac{\mathbf{A}_{\mathrm{pump}}(t)}{c}\right]^2 + v_{\mathrm{KS}}(\mathbf{r}, t)\right\}\right)\right], \tag{11}$$

where $\hat{T}$ is a proper time-ordering operator. The eigenvalues of H_f^{KS} are the Floquet quasi-energies with corresponding Floquet eigenstates (stroboscopic eigenstates). The Floquet states have a time-independent occupation but evolve dynamically in a time-periodic manner. Due to the cycle averaging, the quasi-energies are time independent, which means that, in this picture, there should not be any pump-probe delay dependence of the Tr-ARPES spectra. Such states can be captured by Tr-ARPES in the Floquet regime outlined above. The implications of the Floquet picture for the strong-field regime of solid-state physics remain not fully understood. It has been shown that, due to light dressing, a Floquet sideband can be observed in ARPES [60,91,92] and in the

linear optical response [9,10,48,49,93] as well as in charge transport [94,95]. The sidebands are shifted from the original electronic bands by integer multiples of the driving frequency and are eigenstates of Eq. (11). Floquet dressing by phonons is also possible [96]. It has been argued that such dressing could lead to gap closing and topological phases in certain regimes of laser driving [13,14] or even to free-electronlike states with a parabolic dispersion [12,55,56]. At the same time, this picture can also be utilized as a basis set for calculating highly nonlinear effects such as HHG. Notably, the Floquet picture is not necessarily at odds with the adiabatic Houston picture—if the dynamics are adiabatic, the Floquet quasi-energy bands could simply emerge as the time-averaged
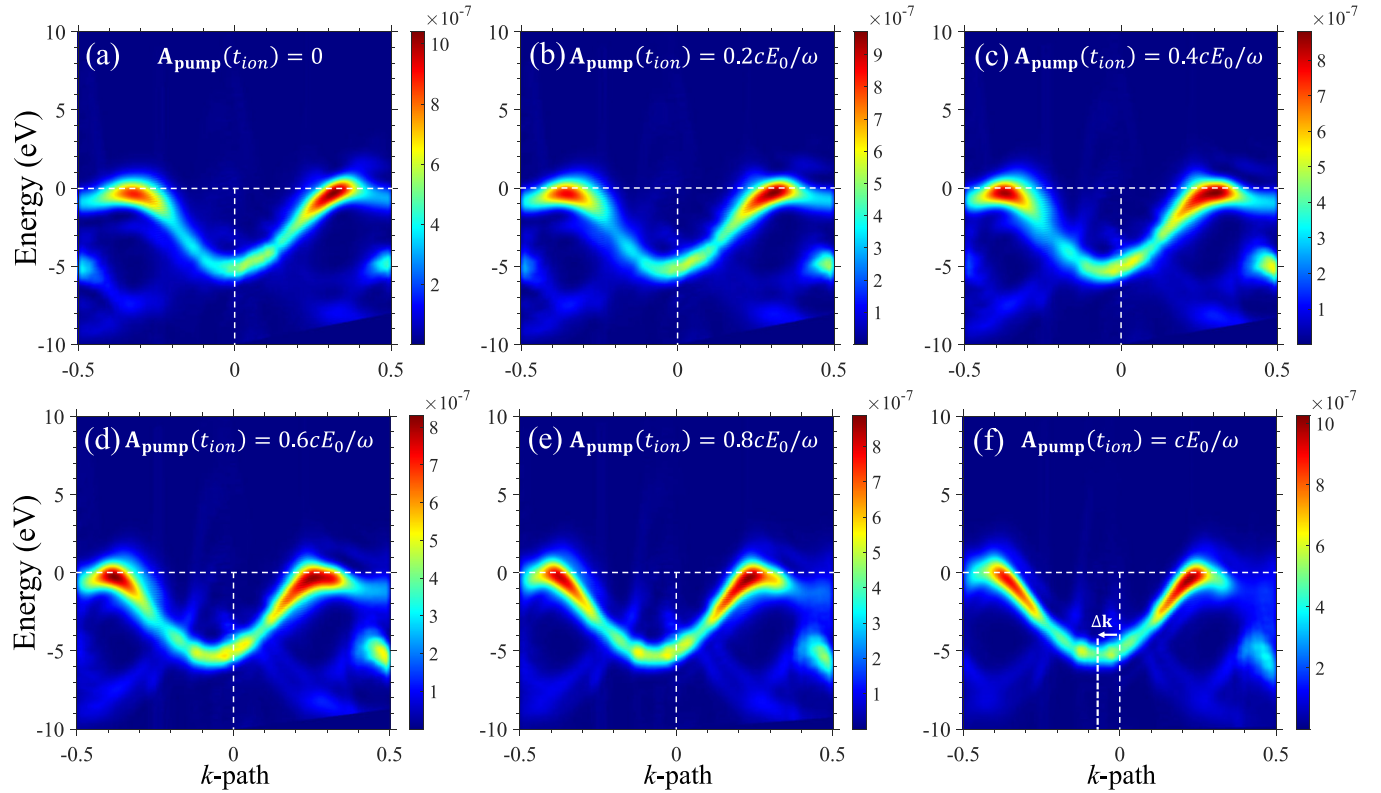
FIG. 4. Time- and angle-resolved photoelectron spectroscopy (Tr-ARPES) in the instantaneous regime vs pump-probe delay. (a)–(f) Tr-ARPES spectra for different pump-probe delays ranging from $\mathbf{A}_{\text{pump}}(t_{\text{ion}}) = 0$ in (a) to $\mathbf{A}_{\text{pump}}(t_{\text{ion}}) = cE_0/\omega$ in (f) (indicated in the figure). Tr-ARPES spectra are calculated for pump parameters of $I_0 = 0.9 \times 10^{12}$ W/cm^2, $\lambda = 2000$ nm. The markings in (f) denote a systematic shift of the band center with the pump vector potential, in accordance with the prediction of the adiabatic Houston states (see text). The effects of continuum state dressing have been removed according to the procedure detailed in Sec. II C. Dashed white lines indicate the positions of the Γ point and valence band edge.

adiabatic Houston bands, where one simply cycle averages $\epsilon_{n,k}^{\text{KS}}(t')$ in Eq. (10).

In between these pictures, one could obtain hybrid states that are neither Floquet states nor instantaneous ones. In other words, there could be some diabatic effects in the light-driven electron dynamics. Recently it has been suggested that such hybrid states lead to gap closings in higher conduction bands [54]. We note that this physical interpretation relies on a different basis expansion of the electronic dynamics, which should give the same results for physical observables as other basis sets. However, since these states have an oscillating form and occupation, they are potentially more difficult to analyze and associate with ARPES spectra.

As a final point, it is also possible that, in extremely strong driving, the standard band picture breaks down. This is the expected behavior if one considers the strong-field approximation that is commonly employed for strong light-matter interactions in atoms and molecules [81]. Essentially, one could imagine that $\mathbf{A}_{\text{pump}}(t)$ in Eqs. (10) and (11) might be so strong (because E_0 is large and ω is small) that it overshadows all other terms in the effective Hamiltonian, leaving the solutions to be approximate eigenstates of the momentum operator (Volkov states). Such behavior would simply lead to a linear dispersion term that is added on top of the field-free bands. Of course, one needs to be careful since that is the same

expected dispersion as that of the continuum acceleration of the electrons. Notably though, the two contributions conceptually differ since, within the solid, this physical situation arises for extreme field values, while in the continuum, it arises for all field values if the electron is sufficiently far from the parent material. Thus, separating the contributions of continuum or bulk dressing would be essential in such a case.

In what follows, we analyze Tr-ARPES from hBN in the strong-field-dressed regime in the context of the above pictures. We will show that, to first order, the instantaneous adiabatic picture prevails as the dominant outlook, even in high field powers and in shorter wavelengths (corresponding to Keldysh parameters up to ∼7).

IV. STRONG-FIELD-DRESSED Tr-ARPES

A. Instantaneous regime

We now present the main results of Tr-ARPES in hBN that is pumped by a strong laser field. As a starting point, Fig. 4 presents Tr-ARPES spectra in the instantaneous regime vs pump-probe delay. The pump field power is set at 0.9×10^{12} W/cm^2 and its wavelength to 2000 nm (corresponding to a Keldysh parameter $\gamma \cong 2.5$). These conditions are usually used to generate high harmonics, transient currents, and possibly even phases of matter. In our case, the HHG
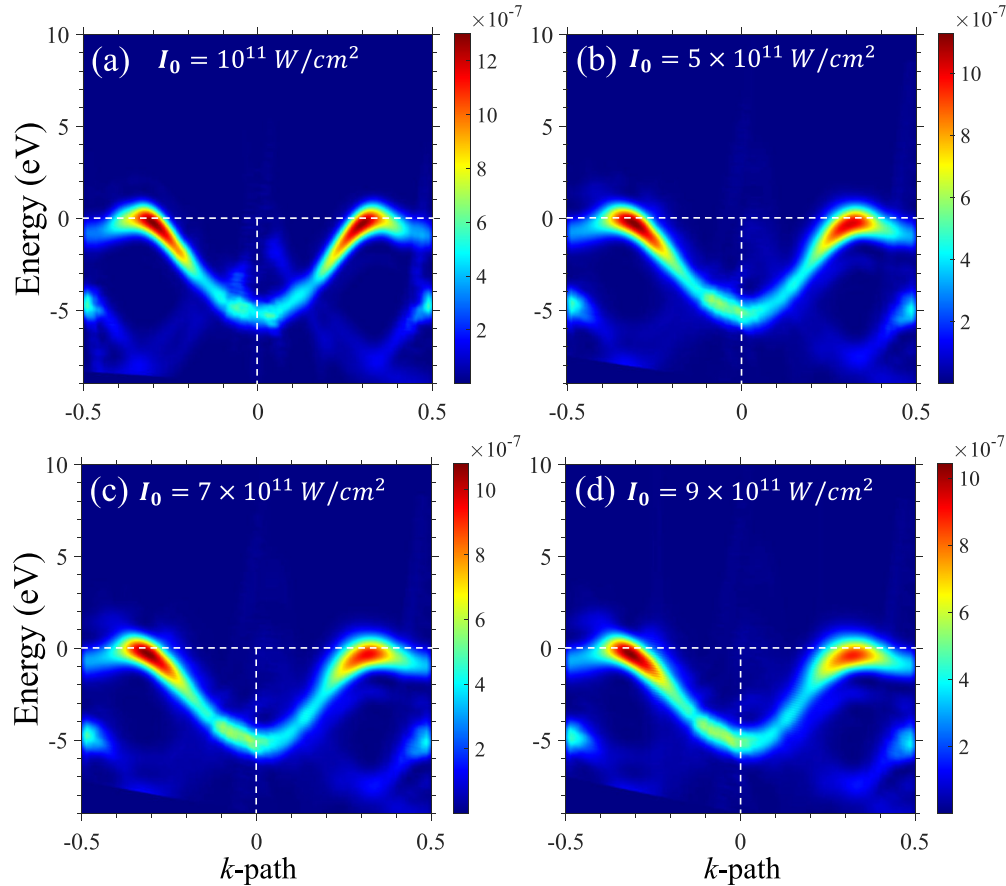
FIG. 5. Time- and angle-resolved photoelectron spectroscopy (Tr-ARPES) in the instantaneous regime vs pump power for $\mathbf{A}(t_{\mathrm{ion}}) = 0$. Pump laser powers are indicated over each figure, and the pump wavelength is taken as $\lambda = 2000$ nm. The effects of continuum state dressing have been removed according to the procedure detailed in Sec. II C. Dashed white lines indicate the positions of the Γ point and valence band edge.

spectrum contains harmonics up to 25 eV, validating that both interband and intraband electron dynamics are present during the interaction of hBN with $\mathbf{A}_{\mathrm{pump}}$ (because harmonic emission with energies above E_g is typically generated by excitations to the conduction band). Figures 4(a)–4(f) show the ARPES spectra vs pump-probe delay for delays ranging from $\mathbf{A}_{\mathrm{pump}}(t_{\mathrm{ion}}) = 0$ [at Fig. 4(a)], up to $\mathbf{A}_{\mathrm{pump}}(t_{\mathrm{ion}}) = cE_0/\omega$ [at Fig. 4(f)]. Note that we focus on the topmost valence band (that includes the VBM at K and K') since, in these conditions, the conduction band occupation is very small and difficult to analyze and since deeper bands are not expected to be strongly affected by the pump laser because they are strongly bounded.

We highlight several main observations in Fig. 4: (i) The band picture generally holds up in these strong fields. (ii) At all pump-probe delays, the bands are very similar to the field-free bands, showing only relatively small deviations. (iii) One main visible effect of the field-dressing is that the valence band (and other deeper bands, not shown) translate along the k axis with the pump-probe delay. This exactly corresponds to the prediction from the adiabatic Houston states—the shift is highlighted in Fig. 4(f) where the pump vector potential is maximized. We verified that this shift indeed corresponds to the value of the vector potential upon the moment of ionization [$\mathbf{A}_{\mathrm{pump}}(t_{\mathrm{ion}})$, the moment at which $\mathbf{A}_{\mathrm{probe}}(t)$ is at

maximum]. (iv) For all delays, one can see a clear asymmetry in the photoemission probability of positive/negative momenta. In other words, the Tr-ARPES spectra are not symmetric under $\mathbf{k} \rightarrow -\mathbf{k}$, even though $\mathbf{A}_{\mathrm{pump}}$ is linearly polarized and even though these states are approximately equally populated with electrons. This is likely a result of the Houston state field dressing that results in a k-dependent phase factor (see Eqs. (14) and (16) in Ref. [52]) that should modulate the ARPES transition matrix elements. Such a phase factor generally differs for different k-points because the trajectory followed by electrons driven in the bands depends on its starting point and on the local band structure around that point. Thus, the ARPES transition matrix elements to the continuum provide clear signatures for the instantaneous Bloch state field-acquired phases and might be used to develop methodology to extract those phases. (v) Lastly, we note that there are effects in the bands that deviate from the Houston state prediction. These will be separately discussed at a later stage.

Next, we explore the intensity dependence of the band-dressing effects. Figures 5(a)–5(d) present the resulting ARPES spectra for a system pumped by 2000 nm light, with varying laser powers, at the pump-probe delay $\mathbf{A}_{\mathrm{pump}}(t_{\mathrm{ion}}) = 0$. For very weak pump power [Fig. 5(a)], the valence band resembles the field-free system [see Fig. 1(c)]. As the pump power is increased, we observe modifications of the bands,
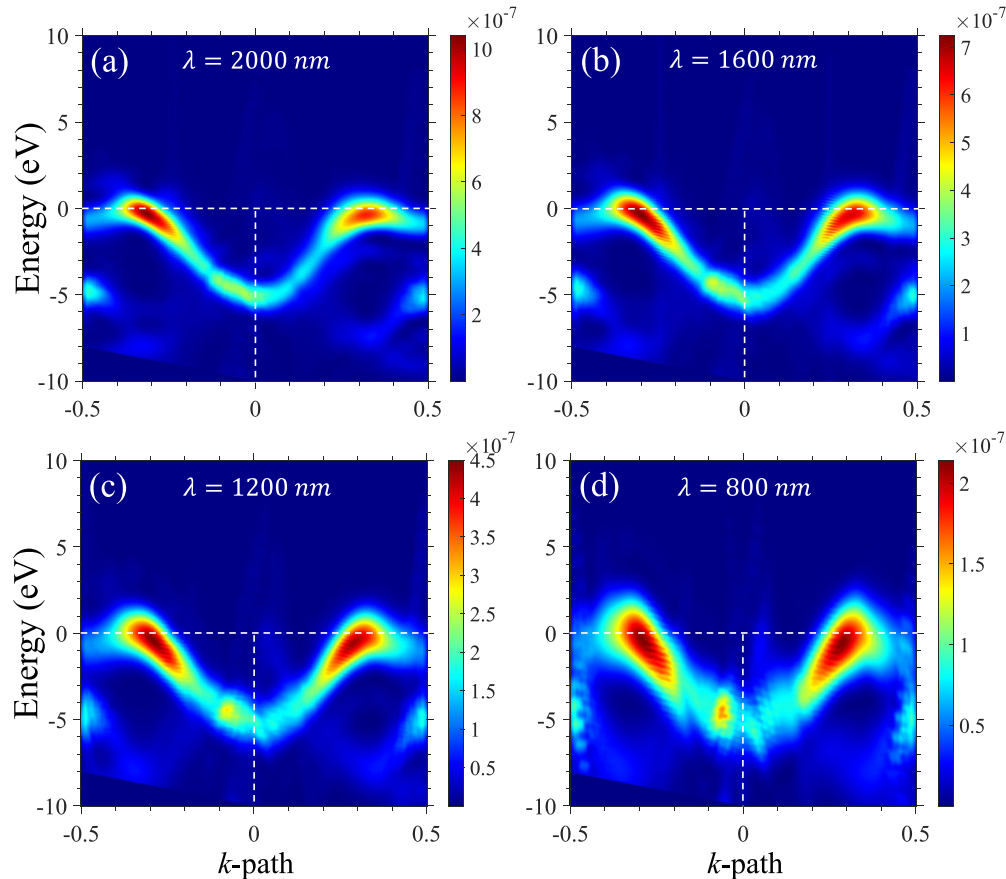
FIG. 6. Time- and angle-resolved photoelectron spectroscopy (Tr-ARPES) in the instantaneous regime vs pump wavelength for $\mathbf{A}(t_{\mathrm{ion}}) = 0$. The pump wavelengths are indicated in each figure, and the pump power is taken as $I_0 = 0.9 \times 10^{12}$ W/cm^2. The effects of continuum state dressing have been removed according to the procedure detailed in Sec. II C. Dashed white lines indicate the positions of the Γ point and valence band edge.

most notably attenuation of the ARPES transition matrix elements as observed also in Fig. 4. However, we also observe slight bending of the valence band near Γ, the origin of which remains unclear. We hypothesize that this effect arises from nonadiabatic electron dynamics with some short-term memory. One point to keep in mind is that, if $\mathbf{A}_{\mathrm{pump}}(t_{\mathrm{ion}}) = 0$, then $\mathbf{E}_{\mathrm{pump}}(t_{\mathrm{ion}})$ is very large, meaning that strong motion of electrons within the bands could also be the cause for such nonadiabatic effects. We emphasize that nontrivial effects such as band bending are well beyond the standard adiabatic picture and should be explored in future work. Overall, the band shape is similar to the field-free bands in all these driving conditions, which largely validates the instantaneous Houston band picture. Similar results are obtained for other pump-probe delays.

Figures 6(a)–6(d) explore the ARPES dependence on the pump wavelength (down to 800 nm) for strong driving conditions. The probe pulse duration in this case is scaled with the relative pump frequency to stay in the instantaneous regime (see Appendix for details). This artificially widens the bands due to time-energy Fourier relations, but the main features are still clearly visible. The conclusion arising from Fig. 6 is that the instantaneous adiabatic picture is valid throughout these driving conditions. In fact, we found it largely valid in the domain of Keldysh parameters $\gamma \sim 1$–7, which is well beyond

the standardly considered adiabatic limit for the system (with $\gamma < 1$). Of course, Fig. 6 still presents some nonadiabaticity effects that become more pronounced for shorter wavelengths, but the original band shape is preserved. This conclusion is valid for all pump-probe delays as well as other laser driving conditions studied here.

B. Floquet regime

Up to now, our calculations validate the instantaneous and adiabatic Houston state picture for analyzing field-dressing effects. However, one might object that these results are biased due to the explored parameter regime for $\mathbf{A}_{\mathrm{probe}}$. That is, because the XUV pulse probes the instantaneous structure of the system (as it is much shorter than the duration of $\mathbf{A}_{\mathrm{pump}}$), a bias toward adiabaticity is created. To address this, we now investigate the Floquet regime, where the probe pulse has a similar duration to one laser cycle of the pump field. In this case, one cannot define a singular moment of ionization for outgoing photoelectrons because they can be ionized at any moment along the pump laser cycle. As such, all photoemission events are coherently summed in time to obtain the resulting Tr-ARPES spectrum. The time periodicity of this procedure manifests as Floquet sidebands in the spectra, which arise from destructive/constructive interference of
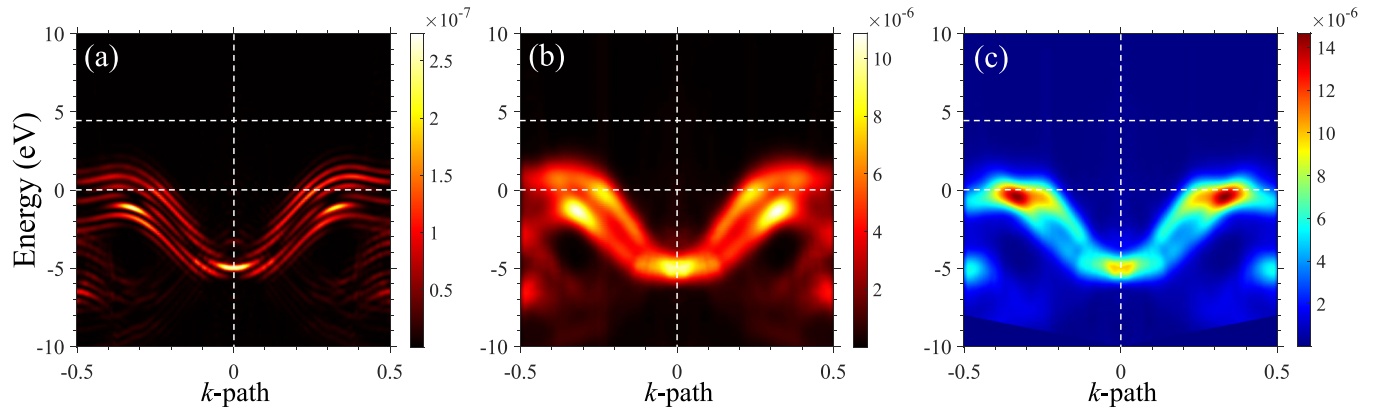
FIG. 7. Time- and angle-resolved photoelectron spectroscopy (Tr-ARPES) in the Floquet regime with different levels of theory. (a) Tr-ARPES spectrum within the Floquet regime, where the spectrum is not corrected for effects of continuum propagation up to the detector. (b) Tr-ARPES spectrum obtained from incoherently averaging the individual spectra vs delay in the same conditions as in (a) but where the probe pulse is in the instantaneous regime. Here, the spectra are averaged over a full laser cycle. Continuum effects of propagation of photoelectron up to the detector are not corrected for. (c) Same as in (b) but where the continuum effects are corrected for. The plots are calculated for pump laser conditions of $I_0 = 0.9 \times 10^{12}$ W/cm^2 and $\lambda = 2000$ nm. Dashed white lines indicate the positions of the valence and conduction band edges and Γ point.

photoemissions from different moments in time. We emphasize that such sidebands are simply a result of the time periodicity of $\mathbf{A}_{\mathrm{pump}}(t)$ and cannot solely validate the Floquet picture for the band dressing (which can only be done by comparing the measured ARPES spectra with the actual Floquet quasi-energy band structure).

The Floquet regime also leads to some numerical issues: Because there is no singular moment of ionization, we cannot fully remove all continuum propagation effects from the spectra (see Sec. II). Even so, we can still determine the origin of the various features appearing in the spectra (band dressing or continuum) by comparing with Tr-ARPES calculations in the instantaneous regime. We achieve this by performing three levels of calculations: (i) the Tr-ARPES calculations within the Floquet regime described above, which still include partial effects of acceleration in the continuum (within the simulation box); (ii) Tr-ARPES calculations that are calculated in the instantaneous regime vs pump-probe delay and are averaged incoherently over a full pump laser cycle. This cycle-averaged spectrum is equivalent to the Floquet calculation only if the electron dynamics are approximately adiabatic and up to the phases of the outgoing photoelectrons. Because it lacks the phase information, it will not lead to Floquet sidebands; and (iii) a calculation of a cycle-averaged Tr-ARPES in the instantaneous regime just as in (ii) but where the continuum effects are removed. By comparing these different levels of theory, we can conclude what are the main band-dressing effects, and as we will show, the adiabatic picture remains valid.

Figure 7 presents calculations of Tr-ARPES spectra with the above-described procedures in the Floquet regime. Figure 7(a) clearly shows the formation of Floquet sidebands with spacing of ω. It also outlines a sizable effect of band widening along the energy axis as well as along the k axis. Widening along the k axis can be viewed as the cycle-averaged result of the bands shifting with $\mathbf{A}_{\mathrm{pump}}(t)$, as observed also in the instantaneous regime. On the other hand, the band widening in the energy axis (and consequential gap

closing by ~ 1 eV) was not observed in the instantaneous regime above, which means that it is either a physical result of Floquet band dressing, or an artifact of continuum propagation. Figure 7(b) shows the cycle-averaged spectrum in the instantaneous regime in similar conditions to Fig. 7(a). Because the spectra are averaged over a cycle incoherently (without phases), no Floquet sidebands appear. Even so, the envelope and main shape of the two spectra are very similar. This indicates that the dynamics are indeed largely adiabatic since the calculation of Fig. 7(b) explicitly assumes adiabaticity. Note that Fig. 7(b) reproduces the ~ 1 eV closure of the bandgap—a peak in photoemission is found 1 eV above the dashed white line that represents the original band edge, whereas standardly, such a peak should be centered at the band edge position. Figure 7(c) further presents the cycle-averaged spectrum that is calculated just as in Fig. 7(b) but where continuum effects are subtracted. It directly shows that the gap-closing effect vanishes, verifying that it was an artifact of the continuum acceleration. The band widening along the momentum axis remains and is a purely adiabatic effect. Similar results are obtained for shorter pump wavelengths. Altogether, we can deduce that the instantaneous adiabatic picture is still widely applicable in these conditions. A cycle-averaged Floquet type of dressing is fully compatible with this Houston state picture, and no additional physical effects are observed.

V. STRONG-FIELD DRESSING WITH COLINEAR ω-2ω FIELDS

At this point, we focus on the nonadiabatic effects observed above and outline one possible procedure to probe them more easily. In the following, we replace the monochromatic pump field in Eq. (4) with a two-color colinearly polarized field:

$$\mathbf{A}_{\mathrm{pump}}^{\omega-2\omega}(t) = f(t)\frac{cE_0}{\omega}\left[\sin(\omega t + \phi) + \frac{\Delta}{2}\sin(2\omega t)\right]\hat{\mathbf{e}}, \quad (12)$$

where ϕ is the relative phase between the two beams, and Δ is the relative amplitude between the beams. Here, $\mathbf{A}_{\mathrm{pump}}^{\omega-2\omega}(t)$
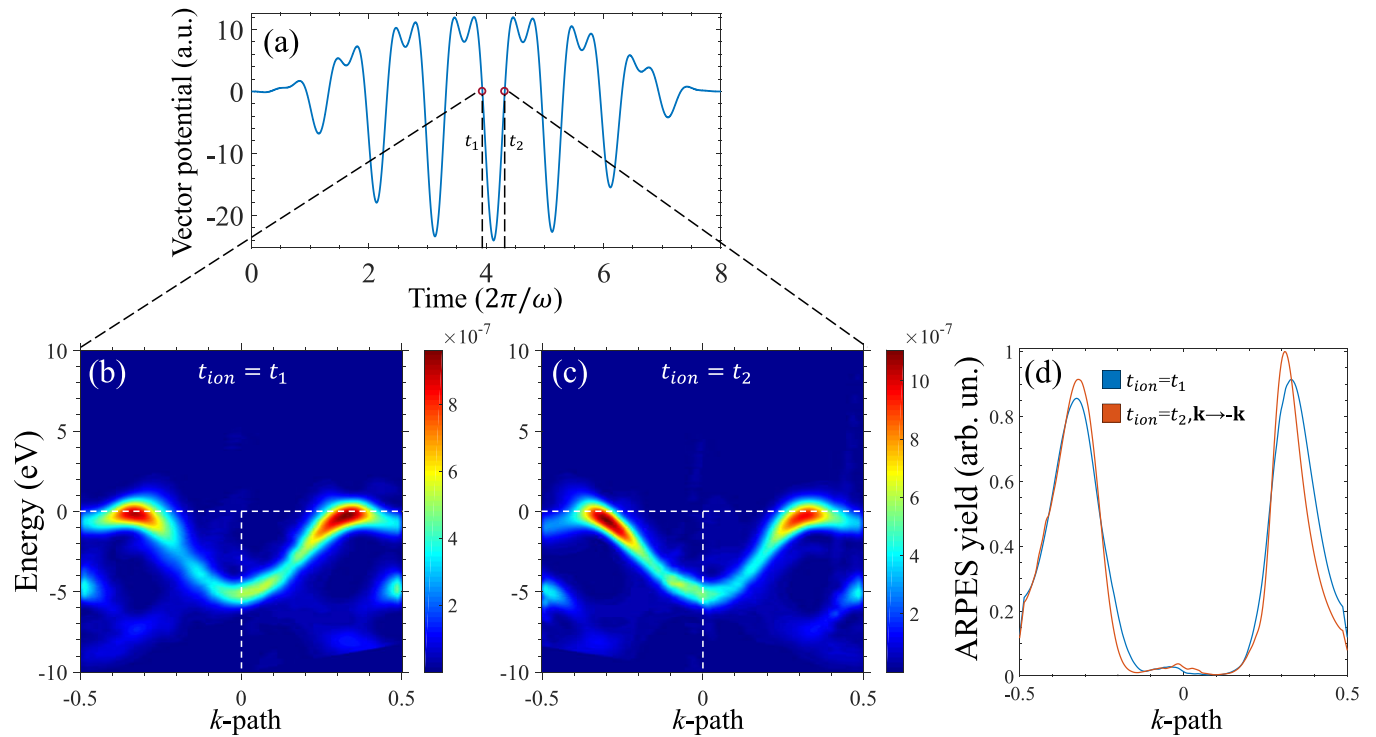
FIG. 8. Time- and angle-resolved photoelectron spectroscopy (Tr-ARPES) in the instantaneous regime with an ω-2ω bichromatic pump [Eq. (12)] for $\Delta = 1$ and $\phi = \pi/4$. (a) Total vector potential vs time showing that the laser field induces time-reversal and inversion symmetry breaking. Two moments in time where the vector potential is zero are highlighted with dashed lines and denoted by t_1 and t_2. While the vector potential is instantaneously zero in both moments, the evolution of the field before them is different, and so is the instantaneous electric field. (b) Tr-ARPES spectrum corresponding to a pump-probe delay where the peak ionization occurs at t_1. (c) Same as (b) but for t_2. Plots calculated with pump parameters $\lambda = 4000$ nm and $I_0 = 2.5 \times 10^{11}$ W/cm^2. The effects of continuum state dressing have been removed according to the procedure detailed in Sec. II C. (d) ARPES yield traces for a fixed photoelectron energy at the valence band maxima [VBM; along the dashed white lines in (b) and (c)], for the two pump-probe delays, but where for t_2 the plot is reflected with $\mathbf{k} \to -\mathbf{k}$. For a monochromatic field, these two curves are identical, whereas the deviation indicates nonadiabatic effects accessible with the two-color approach. Dashed white lines indicate the positions of the Γ point and valence band edge.

describes a two-color coherent field that effectively breaks spatial inversion and time-reversal symmetries [89]. Let us explain why this symmetry breaking is important in the context of nonadiabatic band effects. Nonadiabaticity is most easily observed in pump-probe delays for which $\mathbf{A}_{\text{pump}}(t_{\text{ion}}) = 0$ because, for those delays, the adiabatic picture predicts no modifications (assuming that the contributions of dynamical correlations are negligible). When using a monochromatic field as in Eq. (4), the vector potential vanishes twice per optical cycle (i.e., for every cycle of the pump field there are two pump-probe delays that yield $\mathbf{A}_{\text{pump}}(t_{\text{ion}}) = 0$). Both moments are connected by symmetry. In one of them, $E_{\text{pump}}(t_{\text{ion}}) > 0$, while in the other, $E_{\text{pump}}(t_{\text{ion}}) < 0$, but the absolute value of the field is identical in both. Consequently, the ARPES spectra are identical up to a mirror image—the time-reversal and mirror symmetries in $\mathbf{A}_{\text{pump}}$ connect K to K'. On the other hand, if those spectra were different, one could compare the deviations between them and search for diabatic effects in the dressing dynamics. This is exactly what the two-color field in Eq. (12) and its symmetry breaking implies—there can be up to four temporal moments in a single laser cycle for which $\mathbf{A}_{\text{pump}}^{\omega-2\omega}(t_{\text{ion}}) = 0$. Moreover, even though $\mathbf{A}_{\text{pump}}^{\omega-2\omega} = 0$ in each of those moments, the instantaneous electric field values

$E_{\text{pump}}^{\omega-2\omega}(t_{\text{ion}})$ can be widely different, disconnecting K and K'. This provides additional freedom for observing deviations from the adiabatic bands, especially while scanning the relative beam phase and amplitude.

Figures 8 and 9 present this analysis for two cases. In Fig. 8, we employ $\Delta = 1$, and $\phi = \pi/4$. This leads to a vector potential that has two zeros per optical cycle, the same as in the monochromatic case [see Fig. 8(a)] but with different values for the instantaneous electric fields. Another noteworthy point is that the history of the behavior of the vector potential (and potentially the corresponding electron dynamics) before those moments in time is different between these two temporal moments since the field itself has broken time-reversal symmetry. Indeed, from Figs. 8(b) and 8(c), we observe that the two spectra are not mirror images. Deviations between the images are clear at the K and K' points, where the band curvatures slightly differ and where the ARPES amplitude differs. These are highlighted in Fig. 8(d), which plots the trace of the ARPES spectra for both time delays at a fixed energy, corresponding to the valence band edge. Note that, in Fig. 8(d), the plot is reflected with $\mathbf{k} \to -\mathbf{k}$ for one of the delays, which allows us to directly compare deviations from mirror symmetry. Such effects could be fingerprints of
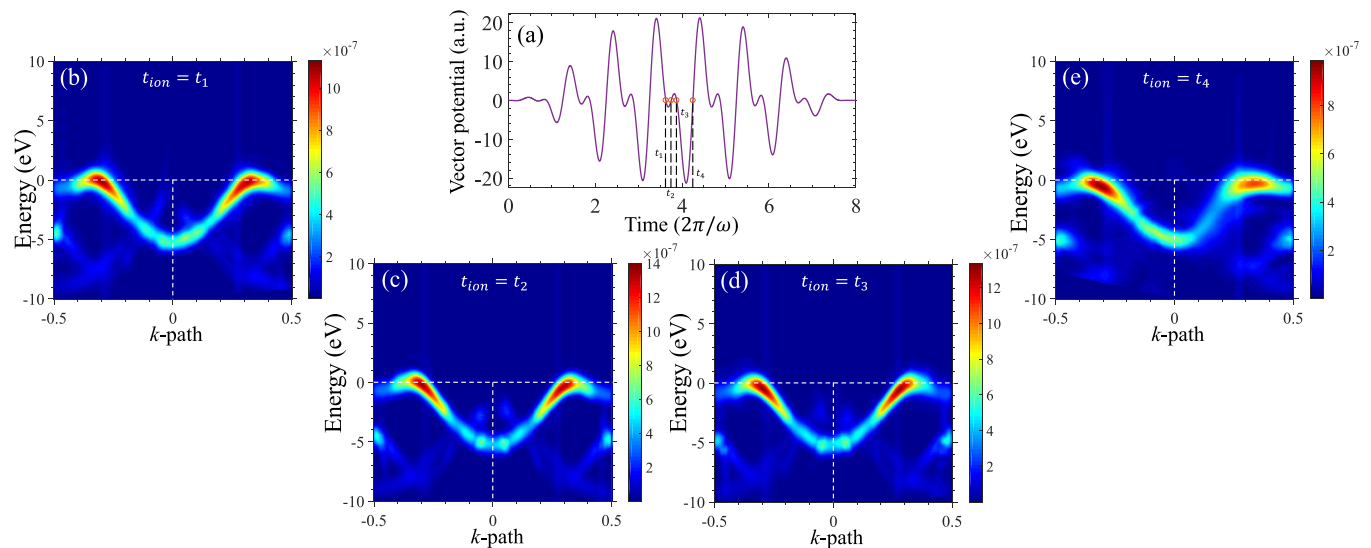
FIG. 9. Time- and angle-resolved photoelectron spectroscopy (Tr-ARPES) in the instantaneous regime with an ω-2ω bichromatic pump [Eq. (12)] for $\Delta = \sqrt{2}$ and $\phi = \pi/2$. (a) Total vector potential vs time showing that the laser field induces time-reversal and inversion symmetry breaking. For these parameters, there are four moments in time where the vector potential is zero, which are highlighted with dashed lines and denoted by t_{1-4}. While the vector potential is instantaneously zero for all moments, the evolution of the field before them is different, and so is the instantaneous electric field. (b)–(e) Tr-ARPES spectra corresponding to a pump-probe delay where the peak ionization occurs at t_1, t_2, t_3, and t_4, respectively. Plots calculated with pump parameters $\lambda = 4000$ nm and $I_0 = 2 \times 10^{11}$ W/cm^2. The effects of continuum state dressing have been removed according to the procedure detailed in Sec. II C. Note that there is some numerical noise around K and K' points for these strong driving conditions causing the vertical lines in the ARPES spectra. Dashed white lines indicate the positions of the Γ point and valence band edge.

short-term memory field-dressing electron dynamics, which are easier to observe with the two-color analysis. We note that, here, E_0 in Eq. (8) is scaled down to correspond to a power of 2.5×10^{11} W/cm^2, such that the total maximal field amplitude (from the coherent superposition of both beams) is close to that used in the previous sections. Moreover, the wavelength of the fundamental period is taken as 4000 nm to make sure that any nonadiabaticity is on equal footing to previous sections (the fastest frequency component in the beam is at 2000 nm).

Figure 9 addresses a regime with $\Delta = \sqrt{2}$ and $\phi = \pi/2$ (the total power is similarly scaled to 2×10^{11} W/cm^2 and the fundamental wavelength to 4000 nm to avoid any bias toward enhanced nonadiabaticity). For these parameters, there are four zeros in $\mathbf{A}_{\text{pump}}^{\omega-2\omega}$ in each laser cycle, which correspond to completely different behaviors in the pumping electric field [see Fig. 9(a) with the highlighted moments in time]. The resulting Tr-ARPES spectra for the corresponding delays are widely different: Figs. 9(c) and 9(d) are remarkably similar to the field-free bands, while Figs. 9(b) and 9(e) show stronger modifications. Specifically, Fig. 9(e) shows strong modifications of the band curvature near K and K'. Since Fig. 9(e) corresponds to the largest instantaneous electric field of these delays and also shows the largest modifications, it suggests that an extension of the adiabatic theory to include the instantaneous electric field [the temporal derivative of $\mathbf{A}_{\text{pump}}(t)$ that also incorporates some nontemporally local effects] might improve the interpretation. Notably, in the Appendix, we show that, in these conditions, dynamical correlations and e-e interactions contribute negligibly to the ARPES spectra and are thus not a main source for the observed deviations from

adiabaticity. Such investigations should be topics of future work.

VI. SUMMARY

To summarize, we explored here Tr-ARPES in a benchmark solid system that is irradiated by a strong pump laser. The resulting ARPES spectra allow us to directly and without additional assumptions observe field-dressed states of matter. This opens the path toward resolving unanswered questions in strong-field physics of solids. For hBN, we determined that the adiabatic bands, as predicted by the Houston state picture [51,52], are valid for a very wide parameter regime. Only weak modifications of the bands were observed in laser powers up to 10^{12} W/cm^2 and down to laser wavelength of 800 nm. Surprisingly, the corresponding Keldysh parameter ranges are up to 7, which is substantially above the standard notion of adiabaticity in light-matter systems. We further validated that this conclusion is upheld even in the Floquet regime, where the ARPES spectra are comprised from coherent motion of electrons in the bands over a full pump laser cycle. Lastly, we put forward a time-resolved approach for observing nonadiabatic effects in bands by measuring Tr-ARPES spectra at pump-probe delays where the instantaneous pump vector potential is zero. With this technique, we showed that there are some interesting effects of band modifications due to light dressing, which can be sensitively probed by pumping the system with a bichromatic ω-2ω field. These results suggest that the adiabatic theory could potentially be amended by adding a term that correlates with the instantaneous electric field, on top of the instantaneous vector

potential. Importantly, in this paper, we do not take upon ourselves the role of formulating theories for the electronic response. In that regard, we simply put forward a possible methodology for distinguishing between theories in a reliable and direct manner, rather than using them as bases for calculations of down-the-line observables (e.g. HHG spectra) and inferring from these whether the theory worked well or not. We hope that these results will stimulate further developments in methodologies.

In this paper, we further validate that the adiabatic band picture should be the correct approach for interpreting strong-field driven dynamics in solids, at least in most cases where the pumping photon energy is far from resonances. This result provides theoretical soundness behind recent efforts for band structure and Berry curvature reconstructions in various systems as well as other ultrafast spectroscopies based on HHG [43–45,47]. At the same time, it remains unclear under what conditions strong modifications or breaking of solid bands could be observed in this regime, as we have not found any indication for it in our simulations. Looking forward, several extensions of this approach present interesting prospects. First, it would be interesting to apply this technique to explore topological systems [20–26], systems driven by topological and chiral light [97–102], strongly correlated systems [28,30,31], nonlinear photocurrents [3–8], systems experiencing symmetry breaking [103,104], and more. Second, Tr-ARPES in the strong-field regime and instantaneous picture presents a unique opportunity to measure photoemission time delays [82,83] to high accuracy, because one can technically time the moment of ionization by mapping it to the instantaneous shifting of the band structure with the pump vector potential. Further development along these lines should be a topic of future work.

APPENDIX

We provide here additional technical details for the calculations performed in the main text as well as some complementary results. The ground state DFT calculations were performed with OCTOPUS code [71–74]. The KS states were discretized on a Cartesian grid with a hexagonal unit cell in the xy plane, corresponding to the primitive cell of monolayer hBN. The transverse z axis was taken to have a total length of 140 Bohr with 70 Bohr vacuum spacing on each side of the monolayer. Lattice parameters and atomic positions were taken at experimental values, and grid spacing was taken to be 0.4 Bohr in all directions. We employed semiperiodic boundary conditions with two periodic dimensions in the monolayer plane (along the lattice vectors) and a nonperiodic z axis with a $12 \times 12 \times 1$ Γ-centered k-grid. Spin degrees of

freedom (as well as spin-orbit coupling) were neglected. Deep core bands were replaced with norm-conserving pseudopotentials [105]. The KS equations were solved self-consistently with a tolerance of $<10^{-7}$ Hartree. Results were converged with respect to grid spacing and k-grid density.

For TDDFT calculations, we employed a complex absorbing boundary in addition to the KS potential described in Eq. (2), with a width of 40 Bohr along the z axis, on both sides of the monolayer, and a $\sin^2(z)$ shape that saturates to a height of -1. This effectively means that photoelectrons have a distance of 30 Bohr to traverse before reaching the onset of the complex absorbing potential, where the numerical detector is also located ($w = 30$ Bohr), and the photoelectron momentum-resolved flux is computed for obtaining ARPES spectra. We employed a time step of $\Delta t = 0.07$ a.u. for the propagation scheme.

The ARPES spectra were obtained with the t-SURFF method as implemented in OCTOPUS [76,77] but where the propagation of the outgoing waves was not performed beyond the numerical detector at $z = w$. This is done to partially remove effects of propagation in the continuum (see main text). The only exception is Fig. 2(a), where a standard t-SURFF approach was utilized including propagation of the Volkov states with the full vector potential. The ARPES spectra were calculated over an energy grid with spacing of 0.01 eV and over a separate k-grid with 72 k-points traversing from $(-0.5, -0.5, 0)$ up to $(0.5, 0.5, 0)$ in reciprocal space (in fractional units of the reciprocal lattice vectors). The resulting spectra were then smoothed with a moving mean filter.

The envelope function of the employed pump laser pulse $f(t)$ was taken to be of the following super-sine form [106]:

$$f(t) = \left[\sin\left(\pi \frac{t}{T_p} \right) \right]^{\left[\frac{|\pi(\frac{t}{T_p} - \frac{1}{2})|}{\sigma} \right]}, \qquad (A1)$$

where $\sigma = 0.75$, T_p is the duration of the laser pulse which was taken to be $T_p = 8T$, where T is a single cycle of the fundamental carrier frequency ($T = 2\pi/\omega$). This form is roughly analogous to a super-Gaussian pulse but where the $f(t)$ starts and ends exactly at 0 which is more convenient numerically. The corresponding FWHM of the pulse is $4T$. The envelope function for the probe laser pulse was taken to have a similar form:

$$f_{\text{xuv}}(t) = \left[\sin\left(\pi \frac{t}{T_{\text{xuv}}} \right) \right]^{\left[\frac{|\pi(\frac{t}{T_{\text{xuv}}} - \frac{1}{2})|}{\sigma} \right]}, \qquad (A2)$$

where T_{xuv} is the total duration of the probe pulse. For the instantaneous regime calculations, we employed $T_{\text{xuv}} = 100(2\pi/\omega_{\text{xuv}})$, which has a FWHM of 2.1 fs. For the calculations in Fig. 6, this duration was linearly scaled with the pump wavelength, i.e., $T_{\text{xuv}} \rightarrow T'_{\text{xuv}} = (\frac{\lambda}{2000 \text{ nm}})T_{\text{xuv}}$. For calculations in the Floquet regime performed in Fig. 7(a), we employed $T_{\text{xuv}} = 400(2\pi/\omega_{\text{xuv}})$, with a FWHM of 8.2 fs (which is a little longer than the pump period at 2000 nm which is 6.7 fs).

Lastly, we show here that the results obtained in the main text are largely independent of dynamical correlations and e-e interactions by comparing results obtained from the full TDDFT calculations (as presented in the main text) with
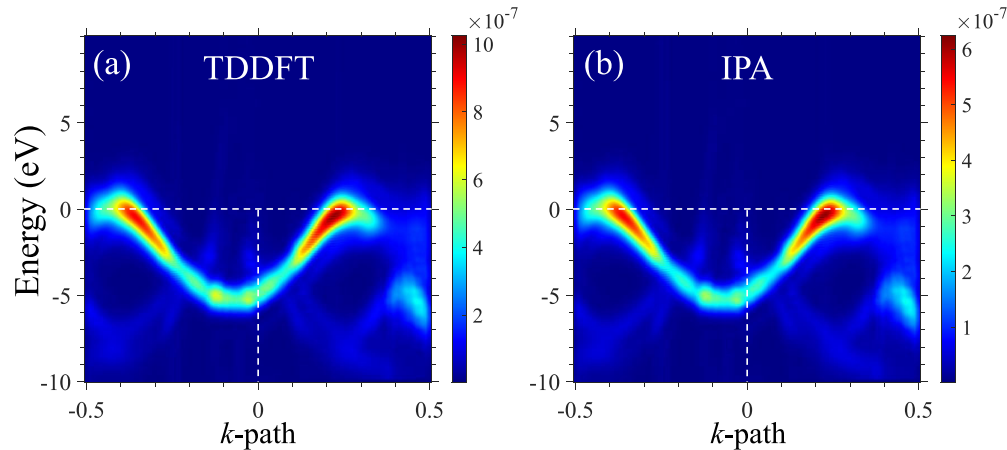
FIG. 10. Time- and angle-resolved photoelectron spectroscopy (Tr-ARPES) in the instantaneous regime comparing the independent particle approximation (IPA) with a full time-dependent density functional theory (TDDFT) calculation. In both ARPES spectra, the system is driven by a pump field with a wavelength of 2000 nm and $I_0 = 9 \times 10^{11}$ W/cm^2, and the pump-probe delay is set such that $\mathbf{A}_{pump}(t_{ion}) = cE_0/\omega$. (a) Full TDDFT calculation. (b) IPA calculation. Dashed white lines indicate the positions of the Γ point and valence band edge.

calculations within the independent particle approximation (IPA). In the IPA, we freeze the dynamical evolution of the Hartree and XC terms in the Hamiltonian, which decouples the equations of motion of all the KS Bloch states and removes any dynamical correlations from the simulations. Such effects could also be considered a source for diabatic effects, regardless of light-dressed states. Figure 10 presents an exemplary calculation of ARPES spectra in the instantaneous regime with the IPA compared with the full TDDFT calculation. The two calculations match extremely well, and similar results are obtained for other laser powers. Thus, we conclude that dynamical correlations are likely not a source of the main deviations from adiabaticity in the bands and that dynamical *e-e* interactions do not substantially affect the Tr-ARPES spectra. We also note that the two calculations differ by an overall factor connected to the photoemission probabilities (ARPES matrix elements). This is likely an effect of a slight renormalization of the KS potential due to ionization in the full TDDFT calculation but does not change the main characteristic features of the response.

[1] S. Ghimire, A. D. Dichiara, E. Sistrunk, P. Agostini, L. F. DiMauro, and D. A. Reis, Observation of high-order harmonic generation in a bulk crystal, Nat. Phys. **7**, 138 (2011).

[2] S. Ghimire and D. A. Reis, High-harmonic generation from solids, Nat. Phys. **15**, 10 (2019).

[3] A. Schiffrin, T. Paasch-Colberg, N. Karpowicz, V. Apalkov, D. Gerster, S. Mühlbrandt, M. Korbman, J. Reichert, M. Schultze, S. Holzner *et al.*, Optical-field-induced current in dielectrics, Nature (London) **493**, 70 (2013).

[4] T. Higuchi, C. Heide, K. Ullmann, H. B. Weber, and P. Hommelhoff, Light-field-driven currents in graphene, Nature (London) **550**, 224 (2017).

[5] C. Heide, T. Higuchi, H. B. Weber, and P. Hommelhoff, Coherent Electron Trajectory Control in Graphene, Phys. Rev. Lett. **121**, 207401 (2018).

[6] F. Langer, Y.-P. Liu, Z. Ren, V. Flodgren, C. Guo, J. Vogelsang, S. Mikaelsson, I. Sytcevich, J. Ahrens, A. L'Huillier *et al.*, Few-cycle lightwave-driven currents in a semiconductor at high repetition rate, Optica **7**, 276 (2020).

[7] S. Sederberg, F. Kong, F. Hufnagel, C. Zhang, E. Karimi, and P. B. Corkum, Vectorized optoelectronic control and metrology in a semiconductor, Nat. Photon. **14**, 680 (2020).

[8] O. Neufeld, N. Tancogne-Dejean, U. De Giovannini, H. Hübener, and A. Rubio, Light-Driven Extremely Nonlinear Bulk Photogalvanic Currents, Phys. Rev. Lett. **127**, 126601 (2021).

[9] M. Lucchini, S. A. Sato, A. Ludwig, J. Herrmann, M. Volkov, L. Kasmi, Y. Shinohara, K. Yabana, L. Gallmann, and U. Keller, Attosecond dynamical Franz-Keldysh effect in polycrystalline diamond, Science **353**, 916 (2016).

[10] T. Otobe, Analytical formulation for modulation of time-resolved dynamical Franz-Keldysh effect by electron excitation in dielectrics, Phys. Rev. B **96**, 235115 (2017).

[11] Q. T. Vu, H. Haug, O. D. Mücke, T. Tritschler, M. Wegener, G. Khitrova, and H. M. Gibbs, Light-Induced Gaps in Semiconductor Band-to-Band Transitions, Phys. Rev. Lett. **92**, 217403 (2004).

[12] H. Lakhotia, H. Y. Kim, M. Zhan, S. Hu, S. Meng, and E. Goulielmakis, Laser picoscopy of valence electrons in solids, Nature (London) **583**, 55 (2020).

[13] Á. Jiménez-Galán, R. E. F. Silva, O. Smirnova, and M. Ivanov, Lightwave control of topological properties in 2D materials for sub-cycle and non-resonant valley manipulation, Nat. Photon. **14**, 728 (2020).

[14] N. H. Lindner, G. Refael, and V. Galitski, Floquet topological insulator in semiconductor quantum wells, Nat. Phys. **7**, 490 (2010).

[15] D. Shin, H. Hübener, U. De Giovannini, H. Jin, A. Rubio, and N. Park, Phonon-driven spin-Floquet magneto-valleytronics in MoS$_2$, Nat. Commun. **9**, 638 (2018).

[16] F. Langer, C. P. Schmid, S. Schlauderer, M. Gmitra, J. Fabian, P. Nagler, C. Schüller, T. Korn, P. G. Hawkins, J. T. Steiner

et al., Lightwave valleytronics in a monolayer of tungsten diselenide, Nature (London) **557**, 76 (2018).

[17] Á. Jiménez-Galán, R. E. F. Silva, O. Smirnova, and M. Ivanov, Sub-cycle valleytronics: Control of valley polarization using few-cycle linearly polarized pulses, Optica **8**, 277 (2021).

[18] M. S. Mrudul, Á. Jiménez-Galán, M. Ivanov, and G. Dixit, Light-Induced valleytronics in pristine graphene, Optica **8**, 422 (2021).

[19] J. Schoetz, Z. Wang, E. Pisanty, M. Lewenstein, M. F. Kling, and M. F. Ciappina, Perspective on petahertz electronics and attosecond nanoscopy, ACS Photon. **6**, 3057 (2019).

[20] D. Bauer and K. K. Hansen, High-Harmonic Generation in Solids with and without Topological Edge States, Phys. Rev. Lett. **120**, 177401 (2018).

[21] R. E. F. Silva, Á. Jiménez-Galán, B. Amorim, O. Smirnova, and M. Ivanov, Topological strong-field physics on sub-laser-cycle timescale, Nat. Photon. **13**, 849 (2019).

[22] A. Chacón, D. Kim, W. Zhu, S. P. Kelly, A. Dauphin, E. Pisanty, A. S. Maxwell, A. Picón, M. F. Ciappina, D. E. Kim *et al.*, Circular dichroism in higher-order harmonic generation: Heralding topological phases and transitions in Chern insulators, Phys. Rev. B **102**, 134115 (2020).

[23] Y. Bai, F. Fei, S. Wang, N. Li, X. Li, F. Song, R. Li, Z. Xu, and P. Liu, High-harmonic generation from topological surface states, Nat. Phys. **17**, 311 (2021).

[24] D. Baykusheva, A. Chacón, D. Kim, D. E. Kim, D. A. Reis, and S. Ghimire, Strong-field physics in three-dimensional topological insulators, Phys. Rev. A **103**, 023101 (2021).

[25] C. P. Schmid, L. Weigl, P. Grössing, V. Junk, C. Gorini, S. Schlauderer, S. Ito, M. Meierhofer, N. Hofmann, D. Afanasiev *et al.*, Tunable non-integer high-harmonic generation in a topological insulator, Nature (London) **593**, 385 (2021).

[26] D. Baykusheva, A. Chacón, J. Lu, T. P. Bailey, J. A. Sobota, H. Soifer, P. S. Kirchmann, C. Rotundu, C. Uher, T. F. Heinz *et al.*, All-optical probe of three-dimensional topological insulators based on high-harmonic generation by circularly polarized laser fields, Nano Lett. **21**, 8970 (2021).

[27] N. Baldelli, U. Bhattacharya, D. González-Cuadra, M. Lewenstein, and T. Graß, Detecting Majorana zero modes via strong field dynamics, arXiv:2202.03547.

[28] R. E. F. Silva, I. V. Blinov, A. N. Rubtsov, O. Smirnova, and M. Ivanov, High-harmonic spectroscopy of ultrafast many-body dynamics in strongly correlated systems, Nat. Photon. **12**, 266 (2018).

[29] Y. Murakami, M. Eckstein, and P. Werner, High-Harmonic Generation in Mott Insulators, Phys. Rev. Lett. **121**, 057405 (2018).

[30] N. Tancogne-Dejean, M. A. Sentef, and A. Rubio, Ultrafast Modification of Hubbard U in a Strongly Correlated Material: *Ab initio* High-Harmonic Generation in NiO, Phys. Rev. Lett. **121**, 097402 (2018).

[31] G. McCaul, C. Orthodoxou, K. Jacobs, G. H. Booth, and D. I. Bondar, Driven Imposters: Controlling Expectations in Many-Body Systems, Phys. Rev. Lett. **124**, 183201 (2020).

[32] C. Shao, H. Lu, X. Zhang, C. Yu, T. Tohyama, and R. Lu, High-Harmonic Generation Approaching the Quantum Critical Point of Strongly Correlated Systems, Phys. Rev. Lett. **128**, 047401 (2022).

[33] G. Vampa, C. R. McDonald, G. Orlando, D. D. Klug, P. B. Corkum, and T. Brabec, Theoretical Analysis of

High-Harmonic Generation in Solids, Phys. Rev. Lett. **113**, 073901 (2014).

[34] O. Schubert, M. Hohenleutner, F. Langer, B. Urbanek, C. Lange, U. Huttner, D. Golde, T. Meier, M. Kira, S. W. Koch *et al.*, Sub-cycle control of terahertz high-harmonic generation by dynamical Bloch oscillations, Nat. Photon. **8**, 119 (2014).

[35] M. Wu, S. Ghimire, D. A. Reis, K. J. Schafer, and M. B. Gaarde, High-harmonic generation from Bloch electrons in solids, Phys. Rev. A **91**, 043839 (2015).

[36] G. Vampa, T. J. Hammond, N. Thire, B. E. Schmidt, F. Legare, C. R. McDonald, T. Brabec, and P. B. Corkum, Linking high harmonics from gases and solids, Nature (London) **522**, 462 (2015).

[37] M. Wu, D. A. Browne, K. J. Schafer, and M. B. Gaarde, Multilevel perspective on high-order harmonic generation in solids, Phys. Rev. A **94**, 063403 (2016).

[38] T. Ikemachi, Y. Shinohara, T. Sato, J. Yumoto, M. Kuwata-Gonokami, and K. L. Ishikawa, Trajectory analysis of high-order-harmonic generation from periodic crystals, Phys. Rev. A **95**, 043416 (2017).

[39] E. N. Osika, A. Chacón, L. Ortmann, N. Suárez, J. A. Pérez-Hernández, B. Szafran, M. F. Ciappina, F. Sols, A. S. Landsman, and M. Lewenstein, Wannier-Bloch Approach to Localization in High-Harmonics Generation in Solids, Phys. Rev. X **7**, 021017 (2017).

[40] C. Yu, S. Jiang, and R. Lu, High order harmonic generation in solids: A review on recent numerical methods, Adv. Phys. X **4**, 1562982 (2019).

[41] L. Li, P. Lan, X. Zhu, and P. Lu, Huygens-Fresnel Picture for High Harmonic Generation in Solids, Phys. Rev. Lett. **127**, 223201 (2021).

[42] L. Yue and M. B. Gaarde, Introduction to theory of high-harmonic generation in Solids: Tutorial, J. Opt. Soc. Am. B **39**, 535 (2022).

[43] G. Vampa, T. J. Hammond, N. Thiré, B. E. Schmidt, F. Légaré, C. R. McDonald, T. Brabec, D. D. Klug, and P. B. Corkum, All-Optical Reconstruction of Crystal Band Structure, Phys. Rev. Lett. **115**, 193603 (2015).

[44] A. A. Lanin, E. A. Stepanov, A. B. Fedotov, and A. M. Zheltikov, Mapping the electron band structure by intraband high-harmonic generation in solids, Optica **4**, 516 (2017).

[45] T. T. Luu and H. J. Wörner, Measurement of the berry curvature of solids using high-harmonic spectroscopy, Nat. Commun. **9**, 916 (2018).

[46] A. J. Uzan, G. Orenstein, Á. Jiménez-Galán, C. McDonald, R. E. F. Silva, B. D. Bruner, N. D. Klimkin, V. Blanchet, T. Arusi-Parpar, M. Krüger *et al.*, Attosecond spectral singularities in solid-state high-harmonic generation, Nat. Photon. **14**, 183 (2020).

[47] Y.-Y. Lv, J. Xu, S. Han, C. Zhang, Y. Han, J. Zhou, S.-H. Yao, X.-P. Liu, M.-H. Lu, H. Weng *et al.*, High-harmonic generation in Weyl semimetal β-WP$_2$ crystals, Nat. Commun. **12**, 6437 (2021).

[48] M. Holthaus, Floquet engineering with quasienergy bands of periodically driven optical lattices, J. Phys. B At. Mol. Opt. Phys. **49**, 013001 (2016).

[49] T. Otobe, Y. Shinohara, S. A. Sato, and K. Yabana, Femtosecond time-resolved dynamical Franz-Keldysh effect, Phys. Rev. B **93**, 045124 (2016).

[50] S. A. Sato, H. Hübener, U. De Giovannini, and A. Rubio, *Ab initio* simulation of attosecond transient absorption spectroscopy in two-dimensional materials, Appl. Sci. **8**, 1777 (2018).

[51] W. V. Houston, Acceleration of electrons in a crystal lattice, Phys. Rev. **57**, 184 (1940).

[52] J. B. Krieger and G. J. Iafrate, Time evolution of Bloch electrons in a homogeneous electric field, Phys. Rev. B **33**, 5494 (1986).

[53] V. Gruzdev and O. Sergaeva, Ultrafast modification of band structure of wide-band-gap solids by ultrashort pulses of laser-driven electron oscillations, Phys. Rev. B **98**, 115202 (2018).

[54] A. J. Uzan-Narovlansky, A. Jiménez-Galán, G. Orenstein, R. E. F. Silva, T. Arusi-Parpar, S. Shames, B. D. Bruner, B. Yan, O. Smirnova, M. Ivanov *et al.*, Observation of light-driven band structure via multiband high-harmonic spectroscopy, Nat. Photon. **16**, 428 (2022).

[55] N. Tzoar and J. I. Gersten, Theory of electronic band structure in intense laser fields, Phys. Rev. B **12**, 1132 (1975).

[56] L. C. M. Miranda, Energy-gap distortion in solids under intense laser fields, Solid State Commun. **45**, 783 (1983).

[57] G. L. Dakovski, Y. Li, T. Durakiewicz, and G. Rodriguez, Tunable ultrafast extreme ultraviolet source for time- and angle-resolved photoemission spectroscopy, Rev. Sci. Instrum. **81**, 073108 (2010).

[58] S. Eich, A. Stange, A. V. Carr, J. Urbancic, T. Popmintchev, M. Wiesenmayer, K. Jansen, A. Ruffing, S. Jakobs, T. Rohwer *et al.*, Time- and angle-resolved photoemission spectroscopy with optimized high-harmonic pulses using frequency-doubled Ti : Sapphire lasers, J. Electron Spectros. Relat. Phenomena **195**, 231 (2014).

[59] M. Puppin, Y. Deng, C. W. Nicholson, J. Feldl, N. B. M. Schröter, H. Vita, P. S. Kirchmann, C. Monney, L. Rettig, M. Wolf *et al.*, Time- and angle-resolved photoemission spectroscopy of solids in the extreme ultraviolet at 500 kHz repetition rate, Rev. Sci. Instrum. **90**, 023104 (2019).

[60] Y. H. Wang, H. Steinberg, P. Jarillo-Herrero, and N. Gedik, Observation of Floquet-Bloch states on the surface of a topological insulator, Science **342**, 453 (2013).

[61] L. Broers and L. Mathey, Detecting light-induced Floquet band gaps of graphene via trARPES, Phys. Rev. Research **4**, 013057 (2022).

[62] A. Damascelli, Probing the electronic structure of complex systems by ARPES, Phys. Scr. **T109**, 61 (2004).

[63] B. Lv, T. Qian, and H. Ding, Angle-resolved photoemission spectroscopy and its application to topological materials, Nat. Rev. Phys. **1**, 609 (2019).

[64] A. Ribak, R. Majlin Skiff, M. Mograbi, P. K. Rout, M. H. Fischer, J. Ruhman, K. Chashka, Y. Dagan, and A. Kanigel, Chiral superconductivity in the alternate stacking compound 4Hb-TaS$_2$, Sci. Adv. **6**, eaax9480 (2022).

[65] S. Beaulieu, J. Schusser, S. Dong, M. Schüler, T. Pincelli, M. Dendzik, J. Maklar, A. Neef, H. Ebert, K. Hricovini *et al.*, Revealing Hidden Orbital Pseudospin Texture with Time-Reversal Dichroism in Photoelectron Angular Distributions, Phys. Rev. Lett. **125**, 216404 (2020).

[66] S. Beaulieu, M. Schüler, J. Schusser, S. Dong, T. Pincelli, J. Maklar, A. Neef, F. Reinert, M. Wolf, L. Rettig *et al.*, Unveiling the orbital texture of 1T-TiTe$_2$ using intrinsic linear

dichroism in multidimensional photoemission spectroscopy, npj Quantum Mater. **6**, 93 (2021).

[67] H. Soifer, A. Gauthier, A. F. Kemper, C. R. Rotundu, S.-L. Yang, H. Xiong, D. Lu, M. Hashimoto, P. S. Kirchmann, J. A. Sobota *et al.*, Band-Resolved Imaging of Photocurrent in a Topological Insulator, Phys. Rev. Lett. **122**, 167401 (2019).

[68] U. De Giovannini, H. Hübener, S. A. Sato, and A. Rubio, Direct Measurement of Electron-Phonon Coupling with Time-Resolved Arpes, Phys. Rev. Lett. **125**, 136401 (2020).

[69] P. Hein, S. Jauernik, H. Erk, L. Yang, Y. Qi, Y. Sun, C. Felser, and M. Bauer, Mode-Resolved reciprocal space mapping of electron-phonon interaction in the Weyl semimetal candidate Td-WTe$_2$, Nat. Commun. **11**, 2613 (2020).

[70] T. Suzuki, Y. Shinohara, Y. Lu, M. Watanabe, J. Xu, K. L. Ishikawa, H. Takagi, M. Nohara, N. Katayama, H. Sawa *et al.*, Detecting electron-phonon coupling during photoinduced phase transition, Phys. Rev. B **103**, L121105 (2021).

[71] M. A. L. Marques, A. Castro, G. F. Bertsch, and A. Rubio, OCTOPUS: A first-principles tool for excited electron–ion dynamics, Comput. Phys. Commun. **151**, 60 (2003).

[72] A. Castro, H. Appel, M. Oliveira, C. A. Rozzi, X. Andrade, F. Lorenzen, M. A. L. Marques, E. K. U. Gross, and A. Rubio, OCTOPUS: A tool for the application of time-dependent density functional theory, Phys. Status Solidi **243**, 2465 (2006).

[73] X. Andrade, D. Strubbe, U. De Giovannini, A. H. Larsen, M. J. T. Oliveira, J. Alberdi-Rodriguez, A. Varas, I. Theophilou, N. Helbig, M. J. Verstraete *et al.*, Real-space grids and the OCTOPUS code as tools for the development of new simulation approaches for electronic systems, Phys. Chem. Chem. Phys. **17**, 31371 (2015).

[74] N. Tancogne-Dejean, M. J. T. Oliveira, X. Andrade, H. Appel, C. H. Borca, G. Le Breton, F. Buchholz, A. Castro, S. Corni, A. A. Correa *et al.*, OCTOPUS, a computational framework for exploring light-driven phenomena and quantum dynamics in extended and finite systems, J. Chem. Phys. **152**, 124119 (2020).

[75] M. A. L. Marques, C. A. Ullrich, F. Nogueira, A. Rubio, K. Burke, and E. K. U. Gross, Time-dependent density functional theory, in *Time-Dependent Density Functional Theory* (Springer, Berlin, Heidelberg, 2003).

[76] A. Scrinzi, *t*-SURFF: Fully differential two-electron photoemission spectra, New J. Phys. **14**, 085008 (2012).

[77] U. De Giovannini, H. Hübener, and A. Rubio, A first-principles time-dependent density functional theory framework for spin and time-resolved angular-resolved photoelectron spectroscopy in periodic systems, J. Chem. Theory Comput. **13**, 265 (2017).

[78] T. E. Glover, R. W. Schoenlein, A. H. Chin, and C. V. Shank, Observation of Laser Assisted Photoelectric Effect and Femtosecond High Order Harmonic Radiation, Phys. Rev. Lett. **76**, 2468 (1996).

[79] L. B. Madsen, Strong-field approximation in laser-assisted dynamics, Am. J. Phys. **73**, 57 (2004).

[80] A. S. Kheifets, The attoclock and the tunneling time debate, J. Phys. B At. Mol. Opt. Phys. **53**, 072001 (2020).

[81] K. Amini, J. Biegert, F. Calegari, A. Chacón, M. F. Ciappina, A. Dauphin, D. K. Efimov, C. F. de M. Faria, K. Giergiel, P. Gniewek *et al.*, Symphony on strong field approximation, Rep. Prog. Phys. **82**, 116001 (2019).

[82] Z. Tao, C. Chen, T. Szilvási, M. Keller, M. Mavrikakis, H. Kapteyn, and M. Murnane, Direct time-domain observation of attosecond final-state lifetimes in photoemission from solids, Science **353**, 62 (2016).

[83] F. Siek, S. Neb, P. Bartz, M. Hensen, C. Strüber, S. Fiechter, M. Torrent-Sucarrat, V. M. Silkin, E. E. E. Krasovskii, N. M. Kabachnik *et al.*, Angular momentum–induced delays in solid-state photoemission enhanced by intra-atomic interactions, Science **357**, 1274 (2017).

[84] M. V. Berry, Quantal phase factors accompanying adiabatic changes, Proc. R. Soc. London. A **392**, 45 (1984).

[85] D. Shin, S. A. Sato, H. Hübener, U. De Giovannini, J. Kim, N. Park, and A. Rubio, Unraveling materials berry curvature and Chern numbers from real-time evolution of Bloch states, Proc. Natl. Acad. Sci. USA **116**, 4135 (2019).

[86] F. H. M. Faisal and J. Z. Kamiński, Floquet-Bloch theory of high-harmonic generation in periodic structures, Phys. Rev. A **56**, 748 (1997).

[87] H. Hübener, M. A. Sentef, U. De Giovannini, A. F. Kemper, and A. Rubio, Creating stable Floquet-Weyl semimetals by laser-driving of 3D Dirac materials, Nat. Commun. **8**, 13940 (2017).

[88] T. N. Ikeda, K. Chinzei, and H. Tsunetsugu, Floquet-Theoretical formulation and analysis of high-order harmonic generation in solids, Phys. Rev. A **98**, 063426 (2018).

[89] O. Neufeld, D. Podolsky, and O. Cohen, Floquet group theory and its application to selection rules in harmonic generation, Nat. Commun. **10**, 405 (2019).

[90] U. De Giovannini and H. Hübener, Floquet analysis of excitations in materials, J. Phys. Mater. **3**, 012001 (2019).

[91] F. Mahmood, C.-K. Chan, Z. Alpichshev, D. Gardner, Y. Lee, P. A. Lee, and N. Gedik, Selective scattering between Floquet-Bloch and Volkov states in a topological insulator, Nat. Phys. **12**, 306 (2016).

[92] S. Aeschlimann, S. A. Sato, R. Krause, M. Chávez-Cervantes, U. De Giovannini, H. Hübener, S. Forti, C. Coletti, K. Hanff, K. Rossnagel *et al.*, Survival of Floquet-Bloch states in the presence of scattering, Nano Lett. **21**, 5028 (2021).

[93] E. J. Sie, Valley-selective optical Stark effect in monolayer WS_2, in *Coherent Light-Matter Interactions in Monolayer Transition-Metal Dichalcogenides* (Springer International Publishing, Cham, 2018), pp. 37–57.

[94] S. A. Sato, J. W. McIver, M. Nuske, P. Tang, G. Jotzu, B. Schulte, H. Hübener, U. De Giovannini, L. Mathey, M. A. Sentef *et al.*, Microscopic theory for the light-induced anomalous Hall effect in graphene, Phys. Rev. B **99**, 214302 (2019).

[95] J. W. McIver, B. Schulte, F.-U. Stein, T. Matsuyama, G. Jotzu, G. Meier, and A. Cavalleri, Light-induced anomalous Hall effect in graphene, Nat. Phys. **16**, 38 (2020).

[96] H. Hübener, U. De Giovannini, and A. Rubio, Phonon driven Floquet matter, Nano Lett. **18**, 1535 (2018).

[97] O. Neufeld and O. Cohen, Optical Chirality in Nonlinear Optics: Application to High Harmonic Generation, Phys. Rev. Lett. **120**, 133206 (2018).

[98] E. Pisanty, G. J. Machado, V. Vicuña-Hernández, A. Picón, A. Celi, J. P. Torres, and M. Lewenstein, Knotting fractional-order knots with the polarization state of light, Nat. Photon. **13**, 569 (2019).

[99] E. Pisanty, L. Rego, J. San Román, A. Picón, K. M. Dorney, H. C. Kapteyn, M. M. Murnane, L. Plaja, M. Lewenstein, and C. Hernández-Garcia, Conservation of Torus-Knot Angular Momentum in High-Order Harmonic Generation, Phys. Rev. Lett. **122**, 203201 (2019).

[100] L. Rego, K. M. Dorney, N. J. Brooks, Q. L. Nguyen, C.-T. Liao, J. San Román, D. E. Couch, A. Liu, E. Pisanty, M. Lewenstein *et al.*, Generation of extreme-ultraviolet beams with time-varying orbital angular momentum, Science **364**, eaaw9486 (2019).

[101] D. Ayuso, O. Neufeld, A. F. Ordonez, P. Decleva, G. Lerner, O. Cohen, M. Ivanov, and O. Smirnova, Synthetic chiral light for efficient control of chiral light–matter interaction, Nat. Photon. **13**, 866 (2019).

[102] G. Lerner, O. Neufeld, L. Hareli, G. Shoulga, E. Bordo, A. Fleischer, D. Podolsky, A. Bahabad, and O. Cohen, Multi-scale dynamical symmetries and selection rules in nonlinear optics, arXiv:2109.01941.

[103] M. E. Tzur, O. Neufeld, A. Fleischer, and O. Cohen, Selection rules for breaking selection rules, New J. Phys. **23**, 103039 (2021).

[104] M. E. Tzur, O. Neufeld, E. Bordo, A. Fleischer, and O. Cohen, Selection rules in symmetry-broken systems by symmetries in synthetic dimensions, Nat. Commun. **13**, 1312 (2022).

[105] C. Hartwigsen, S. Goedecker, and J. Hutter, Relativistic separable dual-space gaussian pseudopotentials from H to Rn, Phys. Rev. B **58**, 3641 (1998).

[106] O. Neufeld and O. Cohen, Background-Free Measurement of Ring Currents by Symmetry-Breaking High-Harmonic Spectroscopy, Phys. Rev. Lett. **123**, 103202 (2019).